Characterization of Optical Coupling and Back-Reflection of Few Mode Fibres

Matthew J. Shipton

Thesis submitted to the Faculty of the
Virginia Polytechnic Institute and State University
in partial fulfillment of the requirements for the degree of

Master of Science
in
Electrical and Computer Engineering

Yong Xu, Chair
Anbo Wong
Yizheng Zhu

June 9, 2015
Blacksburg, Virginia

Keywords: Fibre optics, adaptive optics, mode division multiplexing, fibre bragg grating

Characterization of Optical Coupling and Back-Reflection of Few Mode Fibres

Matthew J. Shipton

(ABSTRACT)

The continued growth of the communications industry has caused interest in mode-division multiplexing (MDM) techniques to flourish in recent years. These techniques allow individual waveguide modes to be used as distinct channels. However, as with any versatile technique, it should also be useful and beneficial to extend its application to other areas. This work concerns itself with an initial conceptual design of a mode-division multiplexing (MDM) enabled optical sensor network that can use modes to interrogate either specific sensors or sensor subsystems, and specifically with quantification and optimizing the injection and detection of the signal of interest. A hypothetical test setup is demonstrated, and the major issue of back-reflection burying the signal of interest is addressed, analyzed, and improved. Improvements in the signal-to-background contrast ratio (SBCR) of approximately 10dB were achieved depending on fibre type and proximal face. Suggestions for extensions to further improve the SBCR as well as for applications of this system are discussed.

Dedication

This work would not have been possible without the ongoing support of many people in my life, and so this is dedicated to them.

My father, John Shipton, for his endless moral support, provided he could figure Skype out.

Victor Wei, Pete Skourbatakos and Richard Labella, who always seemed to show up right when I needed a friend or a distraction. You guys made me feel like I wasn't forgotten. I'll bring you back something nice.

Brennan Thews, who shared in many of the same battles and victories. Remember, Brian, count arm curls in half steps.

Kris Dixon for endless patience in giving me guidance where and when necessary, and where and when necessary removing fish from the percolator. *Ciao ciao pizza Ferrari!*

Gaspode, who calmly and patiently bided his time while I was at the lab all day or getting cramped legs working at my computer. I owe you a car ride.

And finally, the most important person in my life, Anitha Aravindaraman, without whom I never would have been able to do this in the first place. Thank you for putting up with the bad times, rejoicing in the good times, and fighting hard along side me throughout the entirety of this journey. We'll always have banana daiquiris and Battleships. I love you, kiddo.

Acknowledgments

This research was supported with funding by the National Sciences Foundation (NSF CMMI 1400195, 1436335), and this support is gratefully acknowledged.

Contents

List of Figures

List of Tables

Chapter 1

Background and Previous Work

1.1 Fiber Optics

Modes in an Optical Fibre

In the case of some large-core multimode fibres, it is possible to use geometrical optics to find valid solutions (i.e., conditions on variables) that result in energy propagation down the waveguide; however, when core sizes are on the same order as the wavelength of light, the approach instead involves the utilization of both Maxwells equations and the boundary conditions of the dielectric waveguide (optical fibre) to derive the necessary form of the wave equation. [1] For a step-index single-cladding dielectric waveguide, which has cylindrical symmetry, this takes the form:

$$\frac{\delta^2 F}{\delta \rho^2} + \frac{1}{\rho}\frac{\delta F}{\delta \rho} + \frac{1}{\rho^2}\frac{\delta^2 F}{\delta \phi^2} + (\omega^2 \epsilon \mu - \beta^2)F = 0 \tag{1.1}$$

Where F is a placeholder function for the electric (E) and magnetic (H) field profile functions; ρ is the radial component; ϕ is the azimuthal coordinate; ω is the angular frequency of the

lightwave; ϵ and μ are the electric permittivity and magnetic permeability of the medium, respectively; and β is the propagation constant. Taking $k_t^2 = \omega^2\epsilon\mu - \beta^2$ where k_t is the transverse wavenumber, we note that the profile of the fibre is radially symmetric and axially uniform, then we can propose that F has an ansatz of the following form:

$$F(\rho, \phi, z, t) = g(\rho)h(\phi)e^{j(\omega t - k_t z)} \tag{1.2}$$

As the structure does not vary along z, the final term in the equation only results in a phase change. Thus, we can arbitrarily assign z=t=0 and

$$F(\rho, \phi) = g(\rho)h(\phi) \tag{1.3}$$

Then the wave equation becomes

$$h(\phi)\frac{\delta^2 g(\rho)}{\delta\rho^2} + h(\phi)\frac{1}{\rho}\frac{\delta g(\rho)}{\delta\rho} + g(\rho)\frac{1}{\rho^2}\frac{\delta^2 h(\phi)}{\delta\phi^2} + (k_t^2)g(\rho)h(\phi) = 0 \tag{1.4}$$

$$\frac{\rho^2}{g(\rho)}\frac{\delta^2 g(\rho)}{\delta\rho^2} + \frac{\rho}{g(\rho)}\frac{\delta g(\rho)}{\delta\rho} + \rho^2 k_t^2 = -\frac{1}{h(\phi)}\frac{\delta^2 h(\phi)}{\delta\phi^2} \tag{1.5}$$

Here, because either side of the equation is a ratio of equations of different variables, it must be equal to a constant which we will call l^2. Then from inspection, we can further assume $h(\phi)$ takes the form

$$h(\phi) = e^{\pm jl\phi} \tag{1.6}$$

Where $l = 0, 1, 2, 3$ must be an integer to assure the azimuthal component is continuous. Finally and rearranging the equation slightly, we arrive at our final form:

$$\frac{\delta^2 g(\rho)}{\delta \rho^2} + \frac{1}{\rho}\frac{\delta g(\rho)}{\delta \rho} + \left(k_t^2 - \frac{l^2}{\rho^2}\right) g(\rho) = 0 \tag{1.7}$$

This differential equation now describes a family of functions known as Bessel functions [2]: specifically, Bessel functions of the first kind $J_l(ur)$ in the core and a modified Bessel function of the second kind $K_l(wr)$ in the cladding, where

$$u = \sqrt{n_{co}^2 k^2 - \beta^2} w = \sqrt{\beta^2 - n_{cl}^2 k^2} \tag{1.8}$$

Where a is the core radius, and by necessity $J_l(ua) = K_l(wa)$ to ensure the field is continuous across the boundary. Thus we have

$$E_{z,lm} = \begin{cases} AJ_l(u_{lm}r)e^{jl\phi}e^{j(\omega t - k_t z)} & r \leq a \\ CK_l(w_{lm}r)e^{jl\phi}e^{j(\omega t - k_t z)} & r > a \end{cases} \tag{1.9}$$

$$H_{z,lm} = \begin{cases} BJ_l(u_{lm}r)e^{jl\phi}e^{j(\omega t - k_t z)} & r \leq a \\ DK_l(w_{lm}r)e^{jl\phi}e^{j(\omega t - k_t z)} & r > a \end{cases} \tag{1.10}$$

Thus, each solution for a given l and m is itself a solution to the differential equation: the total solution for a given setup is then:

$$E_z = \sum_{l,m} E_{z,lm} \tag{1.11}$$

Valid values for l and m are determined by specific values of β that satisfy the boundary conditions. Importantly, this means two things: energy (light) only propagates through the fibre in discrete, distinct self-reinforcing resonant eigenmodes, and that by definition, the propagation constant β differs for each distinct mode. As the waveguide is dielectric rather than metallic, these exist in four flavours: transverse electric (TE), transverse magnetic (TM), which have electric or magnetic fields with no component in the direction of propagation, respectively; and hybrid modes denoted EH or HE depending on the relative strength of the electric or magnetic field collinear with propagation, respectively. [3]

The exact solution of modes in the fiber is significantly complicated and requires numerical solution; only when the core size is many times greater than the order of the wavelength of light does a geometric optics approach become reasonably accurate. However, if the index contrast is kept small, because of the weakly guiding assumption, most of the modes collapse into degenerate states and allow great simplifications that hold validity under most conditions. These degenerate states are themselves a set of modes (supermodes) known as linearly polarized (LP) modes. For weakly guiding fibres, solutions where an LP mode exists occur where the following dispersion relation (or characteristic equation) is satisfied:

$$u\frac{J_{l+1}(ua)}{J_l(ua)} = \pm\frac{K_{l+1}(wa)}{K_l(wa)} \tag{1.12}$$

If we additionally redefine:

$$U = ua \tag{1.13}$$

$$W = wa \tag{1.14}$$

Then we can define a new third parameter, called the V-number or normalized frequency:

$$V = \sqrt{U^2 + W^2} \tag{1.15}$$

The V-number is a fixed value proportional to the number of valid solutions and thus propagating modes: additionally, since the number of modes is also proportional to the core size, index contrast, and wavelength of propagating light, it can alternately be defined as:

$$V = \frac{2\pi a}{\lambda}\sqrt{n_{co}^2 - n_{cl}^2} = \frac{2\pi a}{\lambda} NA \tag{1.16}$$

If we define W parametrically as

$$W = \sqrt{V^2 - U^2} \tag{1.17}$$

one can graphically solve by plotting both the left- and right-hand sides of the characteristic equation. [2] This is demonstrated in Figure 1.1.

Figure 1.1: Example of graphical solution of modes in a fibre, l=0.

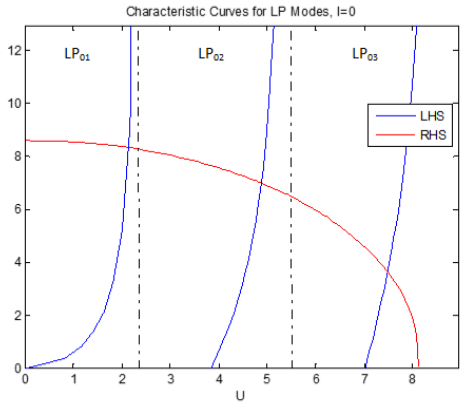

(a) Graphical solution of dispersion relation for order l=0. Intersections between the two lines, representing the LHS and RHS of the transcendental equation, indicate solutions (eigenmodes).

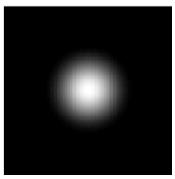

(b) LP_{01} mode pattern.

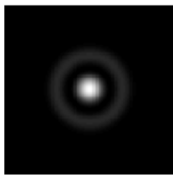

(c) LP_{02} mode pattern.

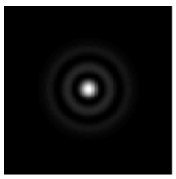

(d) LP_{03} mode pattern.

Figure 1.1a above demonstrates the graphical method for mode determination for Bessel functions of order $l = 0$. Where the blue and red lines intersect a solution exists, and thus a distinct mode; each solution corresponds to the mth root of the Bessel function for that order, thus, $m = 1, 2$ and 3 in this case. This gives rise to the LPlm modes: in this case, LP_{01}, LP_{02} and LP_{03}. The intensity profiles of these modes are given below in Figures 1.1b, 1.1c and 1.1d, respectively.

The effect of the order m on the intensity pattern itself is obvious: it directly corresponds to the number of azimuthal nulls. Further, it is important to note that if the light has a polarization component on both the x and y axes, then all of these modes a second, degenerate mode with the associated perpendicular polarization. However, likewise, we note that for the next order of Bessel functions, $l = 1$, the graphical solution of the characteristic equation takes the following form:

Figure 1.2: Example of graphical solution of modes in a fibre, l=1.

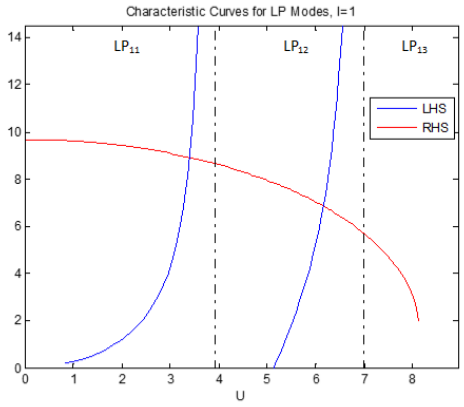

(a) Graphical solution of dispersion relation for order l=1. Intersections between the two lines, representing the LHS and RHS of the transcendental equation, indicate solutions (eigenmodes).

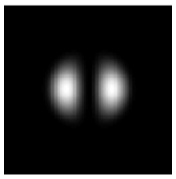

(b) LP_{11} mode pattern.

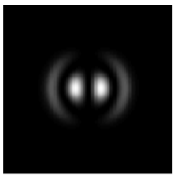

(c) LP_{12} mode pattern.

Thus from the graph in Figure 1.2a we also have two $l = 1$ order modes present in this theoretical fibre, LP_{11} and LP_{12}, whose intensity profiles are also presented in Figure 1.2b and 1.2c.

Thus the effect of the order l on the pattern is likewise obvious: it corresponds to the number of radial nulls on the pattern. Like the $l = 0$ order patterns above, each of these modes also has a corresponding pattern that is polarized on the perpendicular axis, however this time the effect is much more obvious (Figure 1.3).

Figure 1.3: Intensity patterns for mode of order l=1 with orthogonal polarization to those previously presented.

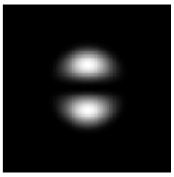

(a) LP_{11y} mode pattern.

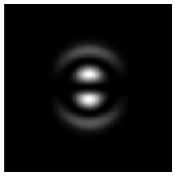

(b) LP_{12y} mode pattern.

If birefringence is present in the fibre, then these two polarizations are not exactly degenerate, making different superpositions of them possible. Additionally, both $l = \pm 1$ is a valid condition, but results in the same solution: therefore, each of these two polarizations is actually two degenerate modes, meaning that a single LP_{11} pattern actually comprises four semi-degenerate mode states. [3]

Further to note is the fact that the value of U for which LP_{11} appears is less than that for LP_{02}: therefore, a mode with only two LP modes will invariably have LP_{01} and LP_{11} (and their respective degeneracies). The order in which LP modes appears is universally fixed across all fibres, and the modes that are present are dependent only on core size, wavelength, and index contrast. Additionally, even though these eigenmodes are discrete and independent, they still superpose with each other, which impacts the pattern seen, for instance, on the distal end of a fibre. Such hybrid modes are typically the rule rather than the exception as intermodal coupling is unavoidable in fibres that have more than one mode, and mode mixing is unavoidable as fibre length increases.

Finally, it becomes clear that if one wishes to only have a single mode present in their fibre, they must choose parameters carefully such that the V-number is 2.405 or less. This is done primarily through restricting core sizes, such that the only difference for a single-mode 980nm fibre versus a single-mode 1550nm fibre is the size of the core.

1.1.1 Mode Division Multiplexing, Adaptive Optics, Turbid Media and the Transmission Matrix

Single-mode fibres (SMFs), that is, fibres that have been designed with parameters to maintain a V-number around, but slightly less, than 2.405 so as to maintain only a single guided LP mode in the fibre, are the du jour medium for long-haul optical communications backbones. [3] This is due to a range of effects, including varying dispersion between modes (due to inherently different propagation constants); therefore, a pulse of light will be received in a

distorted form at the far end of a multimode cable, possibly resulting in unacceptable levels of interference such as intersymbol interference (ISI). Unavoidable intermodal coupling will also aggravate these factors.

However, while the improvements in manufacturing processes and materials that allowed the creation of reliable step-index SMF backhauls hundreds of kilometers long have allowed for the exponential increase in data communications traffic over the last 3 decades, they are quickly approaching a plateau. [4] Shannons theorem, also known as the noisy-channel coding theorem, indicates that the current data rates being reached in SMF hauls are approaching their theoretical limit (the Shannon limit) due to various inherent properties of the physics of light-matter interactions in the material, for instance, Kerr nonlinearities. These effects are intrinsic rather than extrinsic (such as the material losses that previously hexed optical fibres) and so are unavoidable. Various typical means of maximizing traffic rates have been exhausted, such as coding/keying and wavelength division multiplexing (WDM), a corollary to frequency division multiplexing (FDM) utilized in radio waves.

Rather than laying additional, expensive spans of subterranean and submarine cable, current research is investigating means to either improve the potential capacity of new backhauls, or even current ones. In particular, various methods to exploit the only remaining dimension, space, have taken form: true to its name, spatial or space-division multiplexing (SDM) sees implementation through either a multicore fibre (MCF, a structure comprising of multiple single-mode cores in a common cladding) or multimode techniques. [5]

This latter approach has given rise to a specific genre of SDM, known as Mode-Division Multiplexing (MDM). MDM uses each discrete mode state as a distinct communications channel. While not new at all [6], MDM has been gaining popularity in recent years as a method to ameloriate the capacity issue. [5] While this may seem a universal solution to the capacity problem a multimode fibre can easily have thousands of modes at common wavelengths the control and isolation of these channels is far more challenging than at first glance. As control of the modal distributions of energy in the fibre are difficult to control,

and intermodal mixing takes place randomly and constantly within the fibre itself, methods to inject, maintain, and detect a specific modal pattern across an optical fibre remain the primary issues that must be addressed before the technology can even begin to mature.

All manner of adaptive, geometric and Fourier optics have been employed for mode synthesis and detection, including the adoption of many techniques typical of MIMO (multiple-input, multiple-output) in traditional radio communications. [7–11] To keep the number of propagating modes at a reasonable value, few-mode fibres (FMFs) have become an important facet of research. [12–14] Though a somewhat arbitrary category, these fibres will typically be either an SMF operated at a wavelength where it begins to display additional modes, or a specially designed fibre created to elicit the same behaviour at a given wavelength. Such fibres may be designed, for instance, to have a V number close to 3.83, which is the cutoff V-number for the LP_{11} mode, resulting in a fibre with three distinct modes (LP_{01}, LP_{11x}, LP_{11y}).

Increasingly, the use of adaptive optics (AO), and specifically spatial light modulators (SLMs), is rapidly coming to dominate research in the area of MDM. [5, 9, 15] SLMs are typically a variety of liquid-crystal display with pixels that alter the phase of the incident light (available in both transmission and reflection types). Light coupling into a fibre capable of supporting multiple modes will couple most strongly into those modes whose phase and amplitude patterns it matches most closely. [1,16–18] Therefore, an SLM can be used to alter the incident light so that it couples most strongly into the desired modal pattern. [19] A feedback mechanism, such as an instrument providing information on the output modes on the distal end of the fibre, provides the adaptive aspect as an algorithm sequentially adjusts the phase shift of each pixel until the desired output is achieved.

It is important to note that while for relatively short, straight spans of fibre, the input mode may correlate very well to the output mode: long spans, mechanical disturbance, birefringence, macro- and micro-bending as well as intrinsic effects like scattering can causing intermodal coupling to very quickly remove any correlation between input and output

patterns. [3]

Borrowing from seminal work in turbid media imaging and adaptive optics focusing, [20–22] there has also been increased interest in characterizing a few- or multi-mode fibre to determine the relationship between input and output. [23] This is done by treating the fibre as a transmission matrix T, which couples energies in input modes (or pixels, or other discrete metrics) to the respective output, hence:

$$A_{out} = \begin{bmatrix} A_{out,1} \\ A_{out,2} \\ ... \\ A_{out,n} \end{bmatrix} = \begin{bmatrix} A_{in,1} \\ A_{in,2} \\ ... \\ A_{in,n} \end{bmatrix} \begin{bmatrix} T_{1,1} & \dots & T_{1,n} \\ \vdots & \ddots & \vdots \\ T_{n,1} & \dots & T_{n,n} \end{bmatrix} = A_{in}T \tag{1.18}$$

Thus each element in $T_{i,j}$ is the coupling ratio between element $A_{in,i}$ and $A_{out,j}$, whether the elements in A represent discrete modes, detector pixel intensities, or any other valid metric of choice. With a-priori knowledge of T, any output that is possible in the span of A_{out} can be produced with appropriate choices of the elements of A_{in}. While in this context T is defined as the matrix characterizing the relationship between the input at the proximal end of a fibre and the output at the distal end, T can arbitrarily describe such a relationship between any two points.

1.1.2 Fibre Optic Sensors and Sensor Networks

Fibre optic sensors, specifically intrinsic sensors, make use of the variance of optical properties of a fibre due to physical phenomena to measure the amplitude or other features of said physical change. [24] For instance, changes in intensity, polarization, phase, or wavelength (Doppler shift) can be used as mechanisms to measure quantities such as strain, temperature, pressure, or to detect various gases or other substances.

A common method for instance is the creation of a fibre Fabry-Perot (FP) cavity, also known as an étalon. [25] An FP cavity is a gap of differing media commonly air between two other interfaces which are typically partially reflective. This causes interference which modulates both the transmitted and reflected intensity of interrogating light. A change in temperature, for instance, will cause expansion or contraction in the material of the fibres, changing the size of the cavity and thereby the sensor signal amplitude. These are a type of interferometric sensor. [24]

Another common method is the use of fibre Bragg gratings (FBGs) which function under the concept of macroscopic Bragg reflection. [26, 27] Utilizing either a phase mask or an interference setup, a powerful laser is used to inscribe an optical fibre by altering its chemistry, thereby changing the refractive index. The result is a periodic structure that functions as a wavelength-specific dieletric mirror of variable strength.

Fibre optic sensors are powerful because of their minute size, lack of need for external power or electronics, as well as the relative ease of constructing distributed networks: a long fibre can easily have, for instance, multiple FBGs inscribed into it; sequential interrogation of these sensors can then be conducted by either by times-domain methods (reflectometry) if they are all on the same wavelength or wavelength scanning (if the FBGs are tuned to different frequencies).

Fibre sensor networks come in two basic varieties: the reflective and transmissive types. Reflective types launch and receive power on the same end of the system (proximal); transmissive types launch power on the proximal end and receive output power on the distal end. As optical reflection is a significant issue for many fibre optic devices and systems, it is therefore to use a reflective-type network as it can be used as a generalized model. Similar motivations previously led to the development of FC/APC connectors to eliminate back reflection, and in many ways this is an analogous case. A typical setup of a reflective network is given in Figure 1.4.

Figure 1.4: Functional setup of a typical reflective-type fibre sensor network.

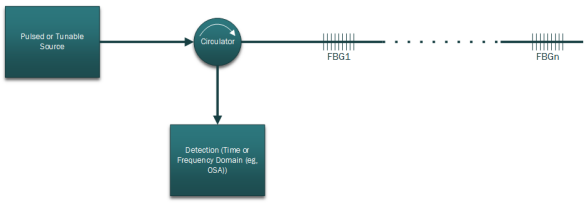

1.2 MDM in Sensor Networks

A powerful aspect of fibre Bragg gratings is their wavelength dependence: for the wavelength of design they function as a dielectric mirror of selectable magnitude, while other wavelengths experience no such reflection. In this way, they can be seen as a stopband filter in transmission, or, alternatively, a bandpass filter in reflection. [28] Furthermore, the fact that propagating modes in a multimode fibre have distinctly different values of propagation constant and therefore wavelength means it is possible to create an FBG that reflects one mode but not another: thus, the response peak of these modes occur at different wavelengths for a given FBG. [29]

As distributed networks therefore already make use of many different methods to multiplex sensors that are already utilized in communications (such as time division and wavelength division multiplexing as above) [30], it is logical then to also expend spatial multiplexing techniques, specifically multimode methods.

Then, it becomes possible to interrogate a distributed system whether using modal selectivity as a mechanism for wavelength scanning, to use the modes as a type of switch to select between different distributed sensor networks by using a demultiplexing scheme such as a phase mask, coupler, or photonic lantern, or furthermore to even use sensors such as FBGs themselves to determine the modal content propagating in a fibre.

However, current reflection-type sensor systems typically make use of either a coupler or optical circulator to inject light into a system and separate it from the reflected signal. [24,30] Additionally, communication systems do not measure the reflected signal (as back reflection is regarded as interference in the communications sense), and the sensors are located at the distal end. [3] This creates a few issues: for one, in order to interrogate a sensor at a given point with the correct mode, we need to know how to excite the necessary mode at the necessary point with our input. This requires knowledge of the transmission matrix T. In cases where the distal end of the fibre is not accessible, this requires us to access modal information from the proximal end of the fibre that will not be kept intact if a circulator or coupler is used. Additionally, use of either of those devices to inject a signal into a fibre could likewise cause loss of the necessary modal information to excite the necessary mode at the sensor. The simplest solution then is direct injection of the necessary excitation input into the same fibre that the sensors are on and subsequent collection of the reflected information back out.

However, a very serious issue exists: typically a distributed FBG system will be weakly reflective to assure adequate power is transmitted through the whole system to interrogate all the sensors. [24,31] This reflectance may be on the scale of a few percent or less. Therefore, the reflected signal exiting the proximal end of the fibre will be very weak, relatively, to the power being injected into it. If the injected power experiences reflectivity on the scale of or larger than that of the gratings, it is very likely the detector will be saturated by this unwanted interference power.

Typically, fibre imaging systems will make use of the raw signal that returns through the fibre. However, these systems typically scan a feature of interest and therefore are interested just the reflected intensity rather than any modal information; additionally, they use several frames of integration to improve signal-to-noise ratio (SNR). [32]

As a result, we ask, what are the sources of reflection interference and how can we ameliorate them?

Chapter 2

Background Sources and Mitigation

2.1 Feasibility Test Setup

Ultimately, the design goal is to design a system that is a hybrid free-space/fibre optic system. The following criteria exist. Per the previous section, in order to interrogate a fibre sensor at a given point A, the appropriate mode must be excited at that point. The injected signal will be subjected to an arbitrary transmission matrix T which could vary at any time due to mechanical stresses, thermal variation, etc. As a result, the injected signal will have to be a variable mixture of the appropriate modes to result in the correct mode at point A. Therefore, adaptive optics will have to be used to select the appropriate modal mixture for injection into the network. Additionally, a feedback mechanism is therefore also necessary, and as stated, we choose this to be the signal reflected back down the fibre from the appropriate sensor. This reflection, hereby known as the signal, will have the same (but reversed) path as the injected power.

To meet these system requirements a set of criteria was therefore developed:

1. The system must have an adaptive optics method on the injection side.

2. The system must be able to both transmit and receive energy (and therefore information) in the form of light mode mixtures along the same path.

3. The system must be able to discriminate the [reflection] signal specifically and modal information in this signal must be preserved.

In order to meet these criteria, the system shown in Figure 2.1, below, was developed.

Figure 2.1: Setup for testing the feasibility of the signal injection/detection system.

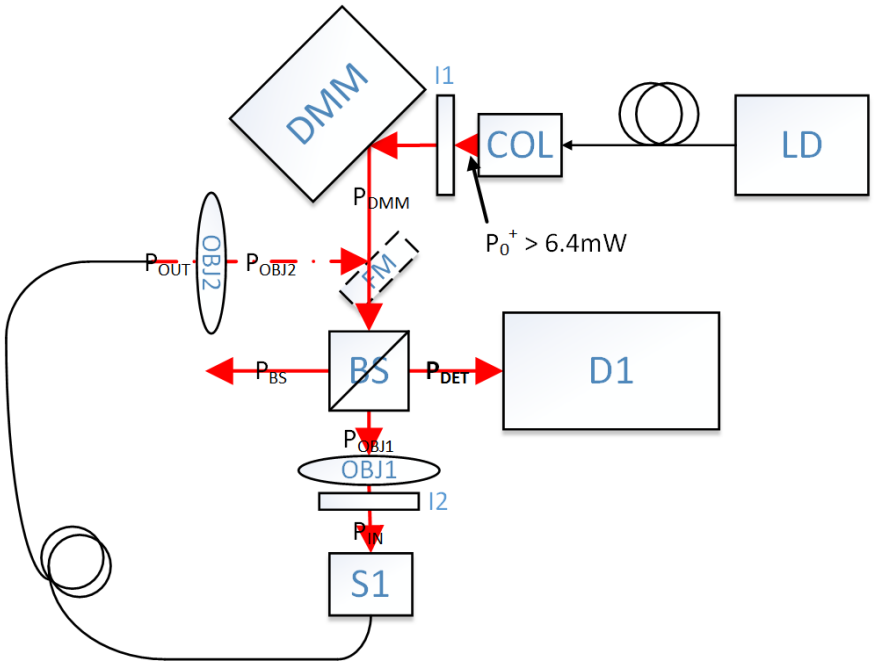

The method of operation of the system in Figure 2.1 is as such: the output of laser diode LD ($\lambda = 660nm$, QPhotonics QFLD-660-10S) is coupled via SMF pigtail to the collimator COL (Thorlabs F810FC-635), expanding the beam to a usable diamter. Iris I1 is used for targeting and alignment purposes. The deformable mirror module DMM (Boston Micromachines Multi-DM) provides adaptive optics mode control to the expanded beam. The beam then continues down its path through the beamsplitter BS (Thorlabs CM1-BP150): half of this

beam is projected in the direction of PD and is not utilized; the other half couples through objective OBJ1 (Mitutoyo 20X Apo-Plan Infinity Corrected Long-Working Distance Lens, f=10mm) and into the fibre sample mounted on stage S1. Iris I2 allows the output of the objective to be trimmed.

Upon reflection, the signal travelling back down the fibre will exit it and follow the orange path shown in the diagram, thus couple through OBJ1 in the opposite direction, and through the beamsplitter BS, out of which half will be directed to the detector D1 and the other half will continue retrograde along the original beampath; the effects of this are not considered in the scope of this work. The detector in our case is a CCD. For targeting purposes, that is, ensuring the reflected signal will be centered on the detector, a flippable mirror FM and second objective OBJ2 allow the beam to be directed down the distal end of a fibre.

For simulation purposes, the distal end of a fibre itself can provide the feedback signal; with an approximate 4% (3.96%) reflectivity of a flat end cleave, this can easily simulate an FBG in the weak reflection regime without increasing system complexity with additional variables. Then, we can inject arbitrary modal mixtures into the front of a fibre sample at S1 and gauge the feasibility of this design using signal data gathered at D1.

Light was coupled into a fibre (OFS Step-Index Two Mode Fibre, $n_{core} \approx 1.462 for \lambda = 633nm$). A free-space power meter was used to measure both the injected power P_{IN} and the power exiting the distal end P_{OUT} to establish the coupling ratio; it was then placed at P_{DET} to measure the power at the detector (CCD) at D1. Two measurements were taken: the first measurement would indicate the sum of the power of the [reflected] signal from the distal end as well as any unwanted reflections within the system (henceforth signal + background power, P_{SB}); then, the distal end of the fibre is immersed in index matching fluid (IMF) which would eliminate most of the back reflection (henceforth signal power, P_{sig}), leaving only the total power of unwanted reflections (henceforth background power, P_{BG}). Then, by subtracting these two components, we can derive the actual signal power and determine the signal-to-background contrast ratio (SBCR), a concept analogous in many

ways to signal-to-noise-plus-interference ratio (SNIR). Thus:

$$P_{sig} = P_{SB} - P_{BG} \tag{2.1}$$

As these are power ratios, the SBCR is easily found then as:

$$SBCR = 10 \log \left(\frac{P_{sig}}{P_{BG}} \right) \tag{2.2}$$

The results of this test are summarized in Table 2.1.

Table 2.1: Summary of coupling and SBCR results for OFS TMF, $\lambda = 660nm$.

	Coupling			Reflections			
Conditions	P_{IN} (mW)	P_{OUT} (mW)	Coupling	$P_{SB}(\mu W)$	$P_{BG}(\mu W)$	$P_{sig}(\mu W)$	SBCR (dB)
Iris Open	1.2761	0.2028	0.1589	29.6	28.23	1.37	-13.1399
Iris Trimmed	0.4533	0.2097	0.4626	15	11.741	3.259	-5.566212
Iris Trimmed	0.25	0.1755	0.702	9.3	6.875	2.425	-4.52561
Iris Closed	0.0311	0.02456	0.7897	1.68	1.32	0.36	-5.64271

Table 2.1 shows several important features. For one, the best coupling occurs when the iris I2 is trimmed down: in fact, the distal power P_{OUT} actually increases when the iris trims injected power P_{IN} to nearly 36% of its maximum: this phenomenon will be significant later. Most importantly, we see that in all cases our SBCR is -4.5dB or worse: this indicates that the system is severely limited by unwanted background power. As signal power P_{sig} is linear with P_{OUT} (or should be), the maximum signal power also occurs where P_{OUT} is at a maximum; however, the background noise P_{BG} decreases with injected power. Therefore the best SBCR occurs at a balance between the two. Finally, we note that since P_{BG} indeed decreases as the iris is trimmed down (thus decreasing the injected power P_{IN}), it is likely that the majority of background does not originate from the components preceding it.

2.2 Origin of the Background Energy

To prove this final detail and determine the source of the background power, we need to determine the contribution each component in the system makes to the total background power. To do this, the system is reassembled from scratch, with power measurements taken at D1 at each step. After using irises I1 and I2 to align the beam centered on the active area of the DM, the beamsplitter is inserted so that measurements may be taken; as well, this first measurement is the contribution of the beamsplitter. The remaining elements are added one by one. The results are summarized in Table 2.2:

Table 2.2: Summary of contributions of various system components to power levels at P_{DET}, $\lambda = 660nm$.

Component	$P_{DET}(\mu W)$
Beam splitter	0.1
Objective	0.75
Iris	0.01
Stage	0.6
Fibre	24.44
Signal	4

Figure 2.2: Imaging of Fibre Face Before and After Source is Activated

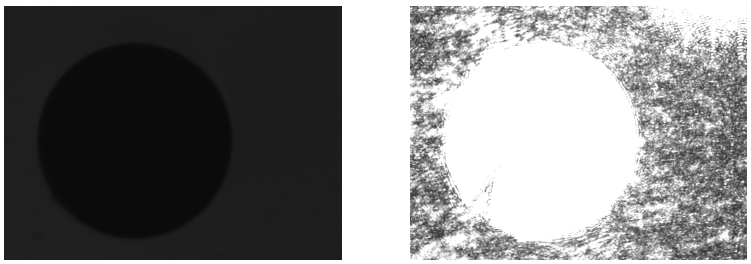

(a) (b)

Here, each element refers to the net change in power detected at the CCD when it is added. In

the case of fibre, this is when the fibre is placed and coupled in front of the lens; signal refers to the power due to back reflection at the distal end. These results show that the majority of the background power is the result of reflection off the fibre face itself. This is also evident in Figure 2.2 which shows an image of the fibre face before (a) and after (b) illumination by the laser. It is important to note, however, that the stage itself is capable of providing this same reflection power even without a mounted fibre; the reason its contribution is so low is because the fibre is positioned with enough lead that it is spatially separate and out of the focal plane of OBJ1.

Thus we know that coupled power is both key and detrimental to our process; the more power we inject and couple, the better the signal power, however, the higher the background noise as well. Even though we can use an iris to trim this somewhat and improve results, -4.5dB is still a poor operating value.

2.3 Solution Analysis

The immediate question becomes: what can we do to mitigate this background power and to improve our SBCR?

An initial reaction may be an anti-reflection (AR) coating. However, while this may be produce some improvement, it is not the optimal solution for a number of reasons. For one, anti-reflection coatings are highly alignment sensitive. As seen in Figure 2.3, the reflectance of an AR coating varies depending on incidence angle. Considering the bare facet is only about 4%, this is significant. This angle must also be taken into account

Figure 2.3: Example of the effect of incident angle versus reflectivity for a single-layer antireflection coating (MgF_2) [33] Edmund Optics. Mgf2 anti-re ection coating performance. Used under fair use, 2015.

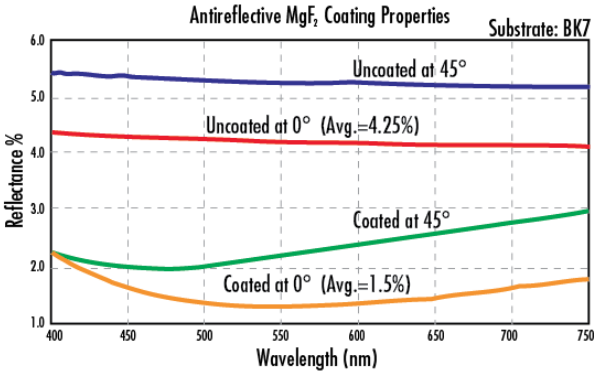

given the NA of the lens. Even at optimal alignment, single-layer coatings such as the MgF_2 given in the figure only improve this reflectance by a factor of 4 (6dB); while multilayer coatings can further improve this to under 1%, they are expensive, narrow-band, degradable, and for non-standard wavelengths require either significant additional investment or expensive and complicated equipment to fabricate.

Potentially, a second solution is the method frequently in use in the area of fibre optic imaging: frame integration. However, this requires several frame iterations to perform (typically between 10-20) and therefore degrades real-time performance. Considering typical DM refresh rates on the order of 1kHz and SLM refresh rates even worse at around 60Hz, this is a serious performance impairment. Finally, if the response is static, the averaging will not highlight the signal, and if it is not static, modal information will be degraded or lost outright. We need a solution that gives single-frame improvement.

The issue is that light that is not coupled into the fibre is either lost in evanescent modes, or reflected. Light that is reflected back within the cone of acceptance defined by the NA of the lens will be collected by the lens and appear as the unwanted background energy. The stage, the face of which is mostly parallel to the face of the lens, is far enough beyond the focal point, it does not greatly contribute to this background noise; however, the fibre, which has a flat cleaved face, must be at or near the focal point in order to couple efficiently. By definition, the light projecting from the lens will fall in a half angle defined by the lens NA; likewise, by the laws of reflection, this same light, when reflected by a flat interface, will therefore always completely reflect back within the cone of acceptance.

As the injected light follows a Gaussian distribution (and assuming the NA of the fibre exceeds or matches the NA of the lens), the outer portions of the light provide less power than the central portion, which is why the iris can be trimmed without significant loss of coupled power (and to some degree, an increase); however, again because the interface is

essentially flat, reflected power is still collected by the lens. The simplest solution then is to angle the interface so that the reflection is either reflected completely out of the collection cone of the objective, or at least so that the iris can be used to filter the reflection without significant loss of coupled power (which would also limit the improvement).

2.3.1 Design and Analysis of the Refraction Chamber

Conceptually then we could also spatially separate the interface from the face of the fibre as well, thereby making the source of the reflection completely spatially independent from the source of the signal. In this case, the basic setup resembles that shown in Figure 2.1.

Figure 2.4: General demonstration of the mechanism of action of the proposed refraction chamber.

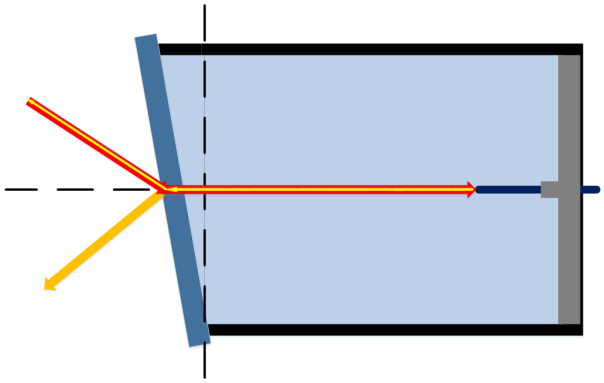

The simplified diagram in Figure 2.4 shows the basic operation of the refraction chamber. The red arrows indicate a ray of incident light and its trajectory; the orange arrows, light that was reflected upon incidence with the chamber window; and the yellow arrows, light that is exiting from the fibre (such as our reflection signal of interest). Upon striking the window, the incident light is refracted. Assuming that the window and fibre have the same refractive index, and that the chamber itself is filled with index matching fluid of the same index, this is the only refraction that will occur. At some angle, the ray will be refracted exactly down the axis of the chamber and directly into the fibre. Thus, light exiting from the fibre down the axis of the chamber will refract at the same angle and follow the same path as the incident light, however in reverse. The light reflected on the face of the window, however, will reflect at twice the incident angle. As the index of the fibre is matched with both the fluid in the body and the window, this is the only reflection that will occur.

Therefore, we can design this chamber as such that the reflected light either falls entirely outside the acceptance angle of the objective or so that it can be filtered out with an iris. Therefore, we must design the chamber so that a) the reflection off the face of the window is not collected by the objective; b) the light ray is coupled directly into the fibre upon refraction. The simplest method is to design the chamber with the fibre fixed along the central axis and the window at a tilted angle θ to the chamber body; then, during setup, the chamber will be fixed at a second angle ϕ to the axis of the objective (thus system) (Figure 2.5).

Then, our design is constrained by the acceptance angle of the objective, thus the numerical aperture, as well as the refractive index of the fibre (assuming we can match it with IMF as well as a window with the same index). Additionally, we must also consider the distance from the front of the window to the face of the fibre, as this must be within the working distance of the lens. As we have chosen a long-working distance lens, in this case, it is 20mm.

Figure 2.5: Key angles to be defined in the refraction chamber design.

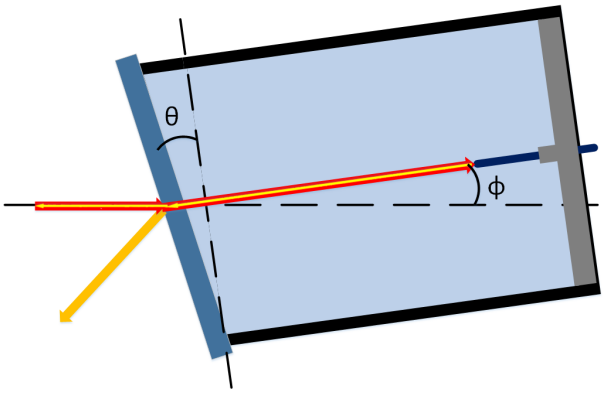

The half-angle of the focal cone of our lens is:

$$\gamma = \arcsin(NA) \tag{2.3}$$

Figure 2.6: Different angles seen by incident cone of light due to tilt of refraction chamber

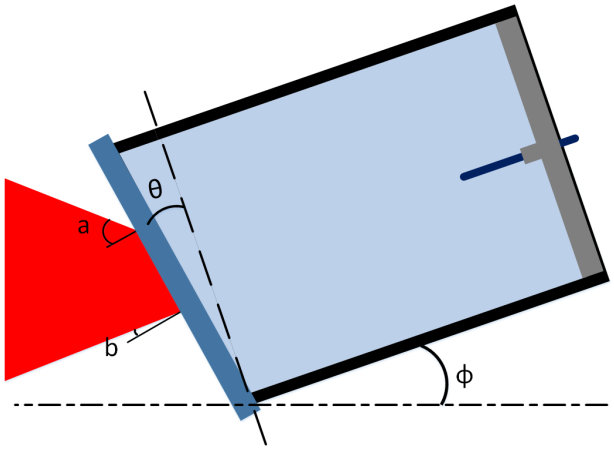

The incident light will be a cone. Assuming that the window is only tilted along one axis, we can effectively reduce this issue to a triangle. On the face of the window, it will make different angles of incidence: angle a

at the top, which will always refract out of the collection angle; and angle b at the bottom, which will only refract if $\gamma < \theta + \phi$. This is shown in Figure 2.6.

In our case, the lens NA=0.42. Then,

$$\gamma = \arcsin(0.42) = 24.83\,\text{deg} \tag{2.4}$$

The angle of refraction of the chief ray of the incident light will undergo refraction per Snells Law. If we assume a nominal value of $n_t = 1.462$ which is typical of silica fibres:

$$n_i \sin(\theta_i) = n_t \sin(\theta_t)$$

$$\sin(\theta_i) = 1.462 \sin(\theta_t) \tag{2.5}$$

In order to assure that the light is completely reflected out of the area of collection of the lens, we require

$$24.83\,\text{deg} < \theta + \phi \tag{2.6}$$

However, there is a clear relationship between all the angles. For instance, the incident angle will be given by

$$\theta_i = \theta + \phi \tag{2.7}$$

$$\theta_t = \theta \tag{2.8}$$

Where the incident angle is determined by the total tilt of the window and chamber, and the transmission angle must be equal to the window tilt in order to travel straight down the tube. In other words,

$$\theta_t = \theta_i - \phi \tag{2.9}$$

Then

$$\sin(\theta_i) = 1.462 \sin(\theta_i - \phi) = 1.462 \left(\sin(\theta_i)\cos(\phi) - \cos(\theta_i)\sin(\phi)\right) \theta_t = \theta_i - \phi \tag{2.10}$$

Thus we can freely choose θ or ϕ. For instance, choosing $\phi = 10\,\text{deg}$,

$$\begin{aligned} \sin(\theta_i) = 1.462 \left(0.9848 \sin(\theta_i) - 0.1736 \cos(\theta_i)\right) &= 1.439776 \sin(\theta_i) - 0.2538032 \cos(\theta_i) \\ 0.439776 \sin(\theta_i) &= 0.2538032 \cos(\theta_i) \\ \tan(\theta_i) = 0.577119 \theta_i &= 29.99\,\text{deg} \approx 30\,\text{deg} \end{aligned} \tag{2.11}$$

Finally

$$\theta_i = \theta + \phi \rightarrow \theta = \theta_i - \phi = 30\,\text{deg} - 10\,\text{deg} = 20\,\text{deg} \tag{2.12}$$

Thus, we can select the window tilt $\theta = 20\,\text{deg}$ and the chamber tilt to be $\phi = 10\,\text{deg}$, which are nice angles, and indeed satisfy

$$24.83\,\text{deg} < \theta + \phi = 30\,\text{deg}$$

As well, we choose a second solution, $\theta = 10\,\text{deg}$: then $\phi = 4.74\,\text{deg}$. Note that this actually does not satisfy $24.83\,\text{deg} < \theta + \phi$: however, the relevance of this choice will be demonstrated shortly.

Both of these chambers were constructed using -inch lens tube, FC connectors and a window made of soda lime ($n = 1.52$); these were then carefully filled with index matching fluid (IMF) ($n = 1.462$). The difference in index between the soda lime window and the rest of the optical apparatus is negligible; the small difference and finite thickness ($t = 1mm$) of the window results in only a small lateral shift in the path. This is easily corrected through alignment.

Furthermore, the window must be large enough to allow all the light from the lens to enter. The light exits the lens with an aperture radius r and forms a cone that is working distance d_w long, with a half-angle that is γ degrees. However, it will encounter the window after distance s, which will cause a refraction that will increase or decrease the half-angle, effectively shortening or lengthening the optical path length. The fibre is spaced a distance d from the front of the window; d must thus be chosen so that the beam width at s is not greater than the window (or tube).

To start, given $\gamma = 24.83\,\text{deg}$ and $d_w = 20mm$, the aperture radius is then $r = 9.256mm$. In the higher-index media ($n = 1.462$),

$$\gamma^{'} = \arcsin(\frac{0.42}{1.462}) = 16.695\,\text{deg} \tag{2.13}$$

Let us assume we are using -inch diameter lens tubing. Then the maximum spot radius is $r^{'} = 6.35mm$, and the maximum spacing the fibre face can be from the window is

$$d = 6.35 \cot(16.695 \deg) = 21.17mm \approx 0.833" \tag{2.14}$$

If we assume the fibre face will be approximately $\frac{1}{2}"(12.7mm)$, which is fairly conservative, then the spot size on the window will be $r^{'} = 3.81mm$ and then the distance to the face of the objective will be:

$$s = d_w - r^{'} \cot(\gamma) = 20mm - (3.81mm) \cot(24.835 \deg) = 20mm - 8.232mm \approx 11.76mm \tag{2.15}$$

We must assure this is far enough away that the overhang from the chamber does not collide with the objective. Given the most extreme tilt of $\theta + \phi = 30 \deg$ and an outer diameter of $d_{OD} = 17.8mm$, the overhang will be

$$\frac{17.9mm}{2} \sin(30 \deg) = 4.45mm \tag{2.16}$$

Which leaves plenty of room. The completed designs are given below in Figures 2.7:

Figure 2.7: Final designs of the refraction chambers.

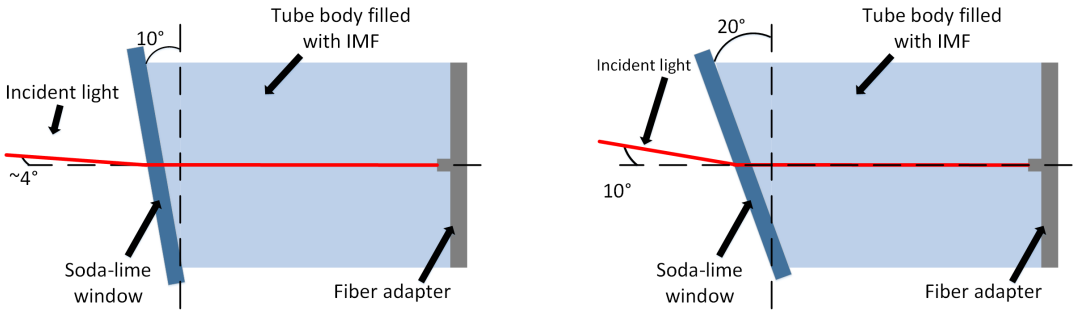

(a) 10 deg window tilt.

(b) 20 deg window tilt.

2.3.2 Testing of the Refraction Chamber

Coupling tests were conducted for both chambers using OFS Two-Mode Fibre ($n_{core} = 1.462 for = 635nm$). For the 10 deg chamber, the following data was gathered in Table 2.3. For reference, the coupling of the chamber is compared to that of OFS Two-Mode Step Index Fibre (TMF). The sample test setup is given in Figure 2.8;

Figure 2.8: Setup for testing the chamber coupling.

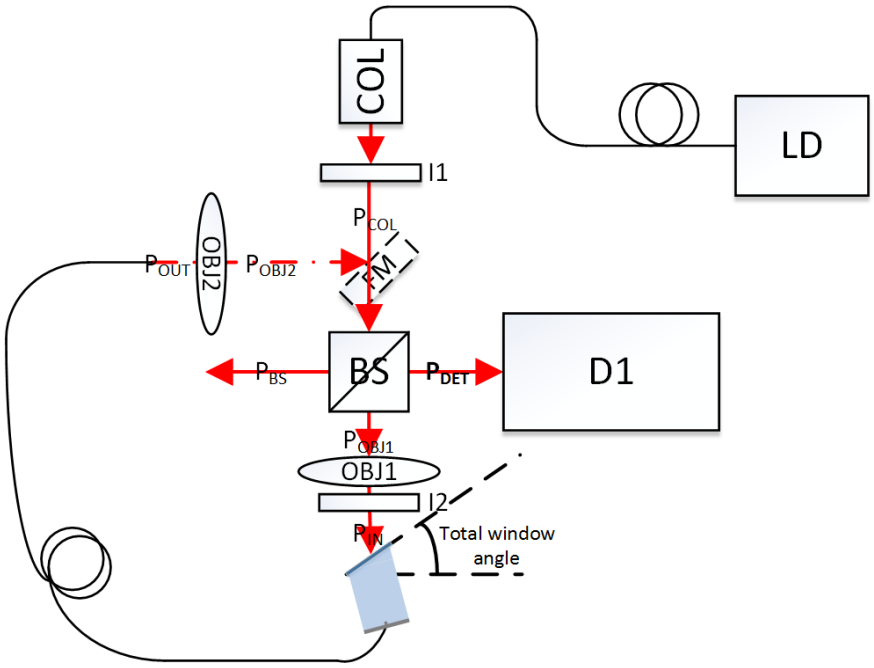

For the 20 deg chamber, the following results were gathered and are displayed in Table 2.4:

Here we note a severe deficiency in the coupling between the two chambers. At their optimal design angle ($\approx$ 14.5 deg and 30 deg for the 10 deg and 20 deg chambers, respectively), the coupling of the 20 deg chamber is less than half of that of the 10 deg chamber; at its best, the 20 deg never even broaches 50%. This in effect means that the signal, which is dependent on coupled power, will be weaker, or alternatively that higher injection powers will be necessary

Table 2.3: Summary of coupling and SBCR results for 10 deg Chamber, OFS TMF, $\lambda = 660nm$.

Iris	Metric	Total Window Angle			TMF
		8	10	14.5	
Open	$P_{in}(mW)$	1.8893	1.88	1.81	1.8
	$P_{out}(mW)$	0.116	0.181	0.175	0.3273
	Coupling (%)	6.14%	9.63%	9.67%	18.18%
Trimmed (1mW)	$P_{in}(mW)$	0.9741	1.0396	1.0148	0.9902
	$P_{out}(mW)$	0.12	0.183	0.175	0.3272
	Coupling (%)	12.32%	17.60%	17.24%	33.04%
Trimmed (0.5mW)	$P_{in}(mW)$	0.5006	0.5025	0.5113	0.5852
	$P_{out}(mW)$	0.106	0.153	0.175	0.3246
	Coupling (%)	21.17%	30.45%	34.23%	55.47%
Trimmed (0.25mW)	$P_{in}(mW)$	-	-	0.2503	0.252
	$P_{out}(mW)$	-	-	0.14	0.185
	Coupling (%)	-	-	55.93%	73.41%
Closed	$P_{in}(mW)$	0.03747	0.04134	0.04153	0.03485
	$P_{out}(mW)$	0.0164	0.0173	0.02945	0.0306
	Coupling (%)	43.77%	41.85%	70.91%	87.80%

to achieve the same P_{sig}. The only benefit of the 20 deg chamber is that the injected power that reflects off the window is guaranteed to be out of the collection angle of the objective lens; however, we have shown above that the actual coupled power into the 10 deg chamber remains very stable for several iris settings. Therefore, it is feasible that this may not even be a factor.

As to why there is a significant difference in coupling, this is easily explainable through the geometry of the two situations. A Matlab script was written to help calculate and illustrate what is going on. Below, in Figure 2.9, is a diagram of the 10 deg chamber. In its current position, the location of the fibre face, taken to be the middle of the back of the chamber, is just beyond the focal point of the coupling LWD objective (thus, too far away).

Table 2.4: Summary of coupling and SBCR results for 10 deg Chamber, OFS TMF, $\lambda = 660nm$.

Iris	Metric	Total Window Angle	TMF
		30	
Open	$P_{in}(mW)$	1.86	1.8
	$P_{out}(mW)$	0.053	0.3273
	Coupling (%)	2.85%	18.18%
Trimmed (1mW)	$P_{in}(mW)$	1.023	0.9902
	$P_{out}(mW)$	0.056	0.3272
	Coupling (%)	5.47%	33.04%
Trimmed (0.5mW)	$P_{in}(mW)$	0.5104	0.5852
	$P_{out}(mW)$	0.043	0.3246
	Coupling (%)	8.42%	55.47%
Trimmed (0.25mW)	$P_{in}(mW)$	-	0.252
	$P_{out}(mW)$	-	0.185
	Coupling (%)	-	73.41%
Closed	$P_{in}(mW)$	0.03912	0.03485
	$P_{out}(mW)$	0.011	0.0306
	Coupling (%)	28.12%	87.80%

Figure 2.9: Diagram illustrating the effect of the tilted interface on focusing of the incident beam, 10 deg chamber.

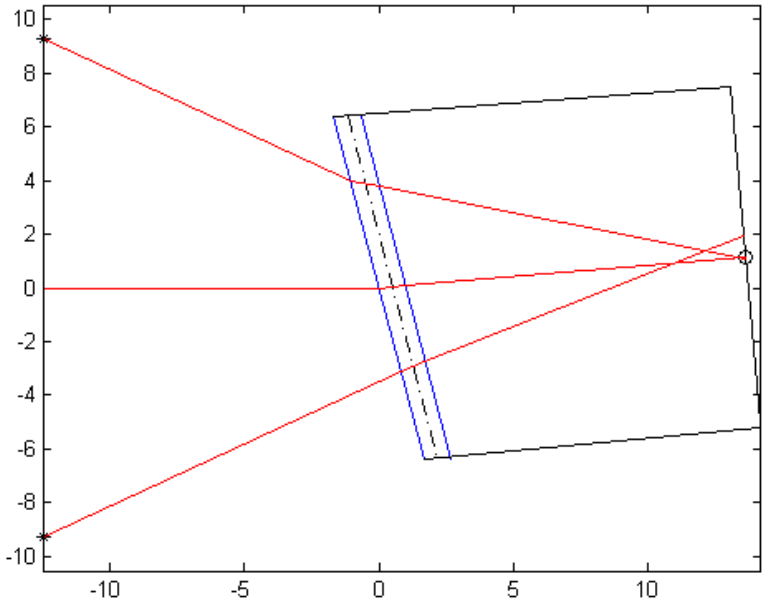

The chief ray from the lens indeed refracts at the correct angle and is directed straight into the fibre. However, the marginal rays from either extreme of the lens encounter the chamber with differing angles, and as a result, refract different amounts. This results in astigmatism within the chamber, which also explains both why two points of best focus were found during the experiment (corresponding to the edges of the circle of confusion) as well as why the chamber coupling differs from that of just a bare fibre.

Figure 2.10: Diagram illustrating the effect of the tilted interface on focusing of the incident beam, 20 deg chamber.

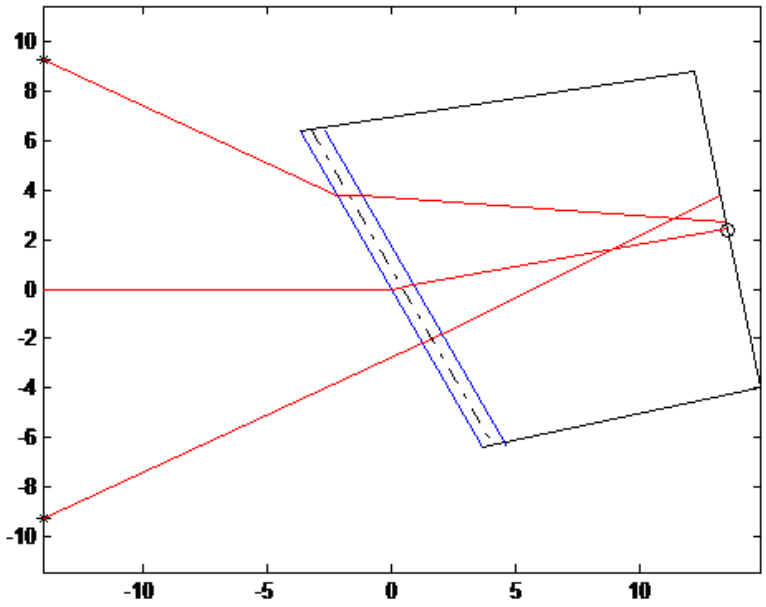

Likewise, the situation for the 20 deg chamber is shown in Figure 2.10. In this situation, the disparity in the angles the marginal rays experience is even greater, and therefore so is the effect of the astigmatism within the chamber. Thus, the chamber will always have poorer coupling; additionally, regarding the injection of modes into the chamber, the mode exiting the objective will undoubtedly be different from that coupling with the fibre; this could complicate modal control at best, or preclude them at worst. Notably, given the effect on light traveling into the chamber, one would also expect the same effect in reverse. If we

reverse the path of the light, we have the diagram shown in Figure 2.11.

Figure 2.11: Diagram illustrating the effect of the tilted interface on focusing of the signal originating from the fibre, 20 deg chamber.

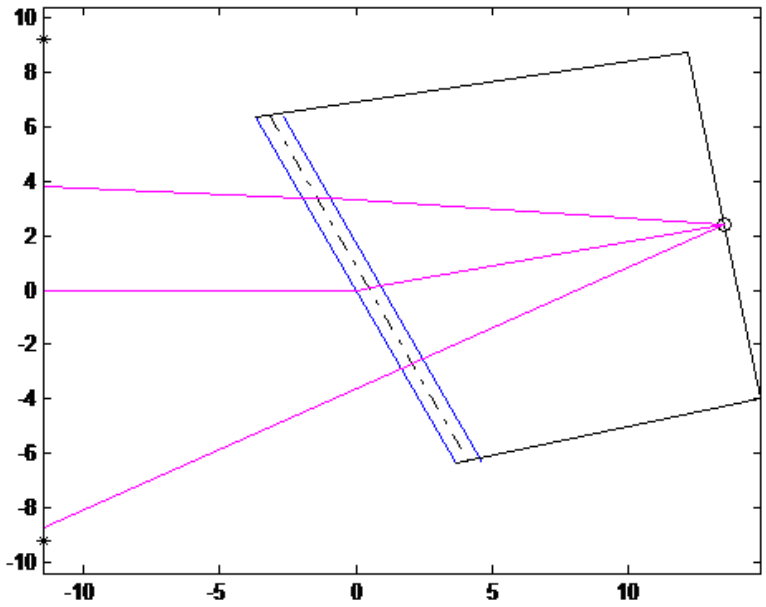

The effect on the signal we wish to detect is now obvious: there is serious distortion of what should be a radially symmetrical signal. Indeed, this effect was noted during testing, as shown in Figure 2.12.

Figure 2.12: Distortion of the signal intensity pattern as position of the chamber changes relative to the objective focal plane.

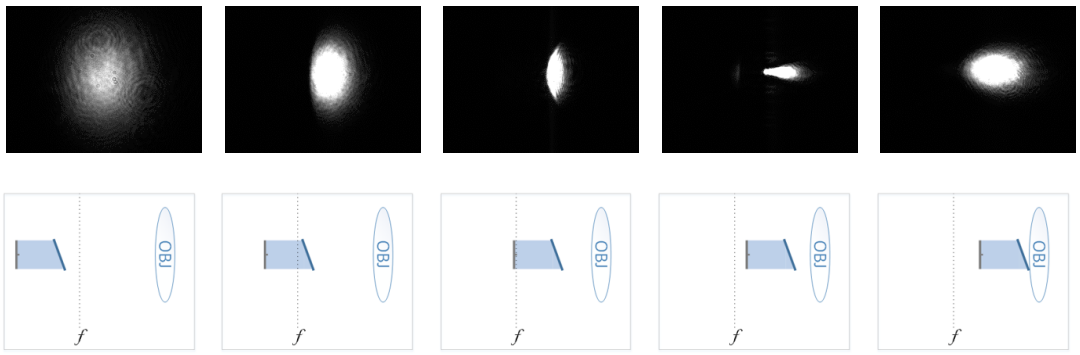

(a) $>> f$ (b) $> f$ (c) $= f$ (d) $< f$ (e) $<< f$

Here we see that the shape of the signal is distorted and ovoid; as it passes the focal point, it twists, and becomes ovoid on a different axis. Specifically, we can see how sharply it is limited on one side (the left in 2.12b), coinciding with the asymmetry suggested in the previous diagram. As to why the change of axis takes place, it is possibly that the tilt of the chamber is not entirely aligned on one plane of the lens.

Figure 2.13: Diagram illustrating the effect of the decreased fibre face-window face separation on distortion of injected signal, 10 deg chamber.

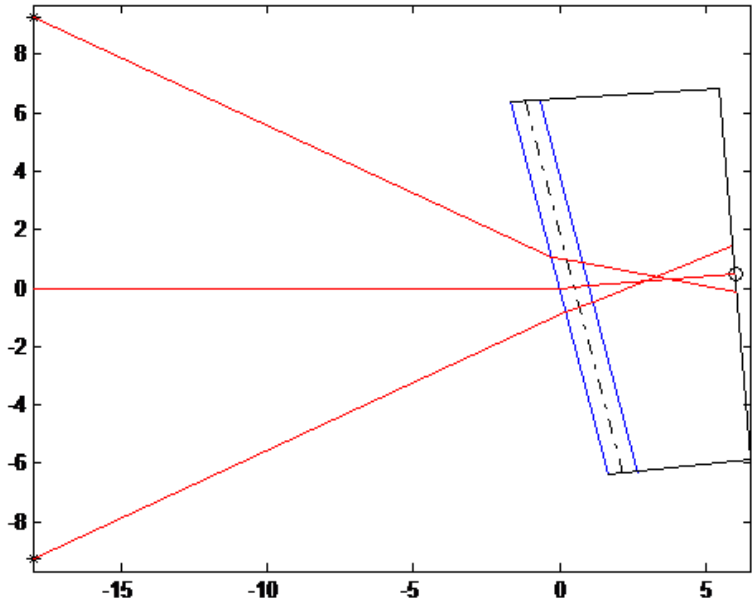

Finally, we consider the case where the separation between the front of the window and the face of the fibre approaches zero. Notably, if we move the fibre closer, such as in Figure 2.13, where the fibre is now located $d = 5mm$ rather than the $12.7mm$ above, the astigmatism is notably reduced. Then, as $d \to 0$, we should expect that the astigmatism itself disappears, because the exact point where the rays encounter the interface is the same as where they are coupled to the waveguide. While some energy may be lost (notably if the angle of incidence for the marginal ray exceeds the acceptance cone of the fibre), it should have a greatly improved coupling and signal image fidelity. Practically speaking, this reduction is simply the case of an Angled Physical Contact (APC) cut fibre. This reduction is given in Figure 2.14. If this is true, then by logical extension, we should expect an APC cable to have better performance than the chamber, and more importantly, the best performance out of all options.

Figure 2.14: Diagram illustrating the effect of the decreased fibre face-window face separation on distortion of injected signal, 10 deg chamber.

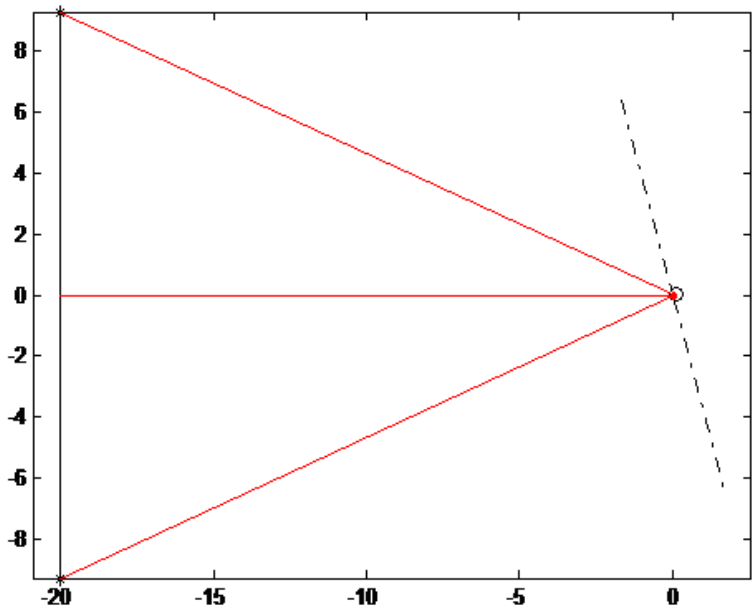

Chapter 3

Testing and Comparison of Methods

3.1 Test Setup

Given the results of the previous chapter we now wish to test the performance of the reflection chamber with regard to a few criteria. For one, we wish to ascertain whether or not it indeed offers an improvement in the Signal-to-Background-Contrast Ratio (SBCR), effectively an analogous quantity to SNIR, compared to the basic case of a flat cleave for the proximal face. Based on the geometric optical analysis of the last section, we also wish to compare it against an APC fibre, which should theoretically be the extreme case of the fibre face coinciding with the window. If the effect of the spatial mismatch between the incident field and fibre mode is indeed what causes coupling problems, then the APC fibre should theoretically have the best performance.

Table 3.1: Fibre Types to Be Tested, $\lambda = 660nm$.

Fibre Type	V-number (660nm)
SM600	2.05
780HP	2.72
980-5.8-125	3.59
SMF28e+	5.46

Finally, we wish to test this for multiple types of fibres that represent various V numbers and therefore different degrees of multimodality. These fibres are summarized in table 3.1, above.

Figure 3.1: Setup for testing and comparing various proximal face conditions for multiple fibre types and distal end conditions.

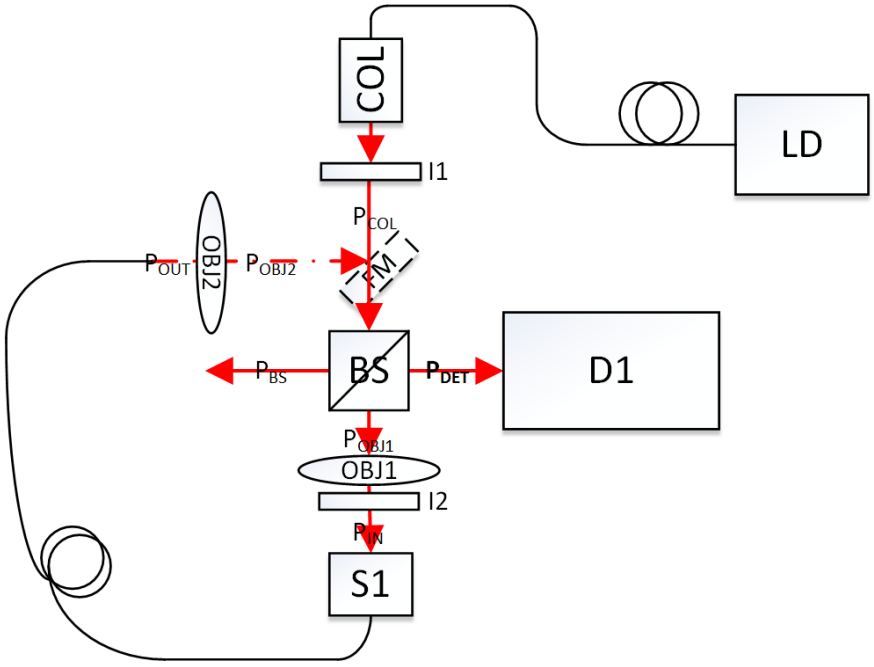

The testing procedure utilizes a setup very similar to those previously used, as shown in Figure 3.1. In this setup, however, the deformable mirror has been removed because it is

not essential to our setup and introduces therefore an unnecessary step. Now, I1 is used to trim the output of the collimator to a radius just greater than that of the objective (thus completely filling it); this, along with control of the lasing current of the laser diode has been used to ensure the same injected power into the objective as with the deformable mirror setup. I2 is again used for trimming the output of the LWD objective into the system, as well as acting as the spatial filter for the reflection.

3.2 Procedure

The testing cases are as follows. The proximal end has four possible different cases: flat cleave, 10 deg chamber, FC/APC, and in at least one case, FC/PC for comparison. In each case, the appropriate sample is loaded into a holder on the stage S1 and aligned with OBJ1 to couple light in. In each case, there are three distal end cases: bare cleave, index matching fluid, and fibre mirror. The purpose behind each of these is as follows: the bare cleave acts as to simulate a relatively weak grating (approximately -14dB); the index matching fluid should act as essentially no reflection, therefore allowing us to derive the actual signal power at the detector through inference; and the fibre mirror acts as a theoretically perfect reflection ($0dB$ reflection). Each one of these tests is repeated for one of several different types of fibre: SM600 (single mode, $V \approx 2.4$), 780HP (two mode , $V \approx 2.72$), 980-5.8-125 (few mode, $V \approx 3.86$), and SMF28e+ (multimode, $V \approx 5.46$). These fibres were selected to test under a range of levels of multimodality at our wavelength ($\lambda = 660nm$). Finally, each test was repeated multiple times for both a fully open iris as well as an iris trimmed to various degrees.

Therefore, the following procedure was used. For a given fibre type and proximal end case, first light was back-coupled through OBJ2 into the distal end of the fibre to assure proper targeting on the sensor (CCD and/or power meter). Then, the flippable mirror was lowered, and light was coupled into the proximal end through OBJ1 until the power at the distal

end (P_{OUT}) was maximized. The power at P_{DET} was then measured. The distal end would then be immersed in index matching fluid to remove any reflection occurring because of the distal cleave, and again P_{DET} was measured. The distal end is then cleaned, recleaved and once again P_{DET} is recorded; this also serves to verify that coupling does not significantly change due to mechanical disturbance of the fibre. The distal end is then spliced using a fusion splicer (Fujikura FSM-40S) to an appropriate fibre mirror, and P_{DET} is recorded. Finally, the splice is broken, the distal end is again recleaved, and P_{DET} is again verified and measured. This procedure is repeated multiple times for each proximal end case, for both open and trimmed iris, and each fibre type.

Between tests, the intrinsic background noise present in the system itself was regularly measured; that is, the power P_{DET} when the stage S1 was not present. In particular, it was measured for two extremes: the iris I2 fully open and fully shuttered. These values, summarized in Figure 3.2, allow us to derive the amount of background power that is due to reflection from the proximal face. As expected, the intrinsic system background power is higher when the iris is closed; however, it is not out of the errorbars of the open iris case, so while these differences are taken into account, we can consider them statistically the same.

Figure 3.2: Average of intrinsic background power (eg no stage, fibre) for both open and closed iris cases.

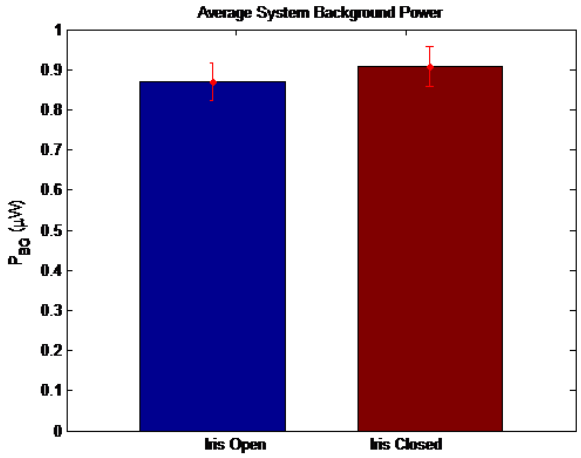

3.3 Analysis of Results

The following details the analysis of data gathered from this testing procedure. As our interest is in multimode systems, even though data was gathered for all fibre types, we present the data for 780HP, which is the simplest multimode fibre. Remaining data and graphs can be found in Appendix A.

Figure 3.3: Plot of raw coupling data for 780HP, all cases.

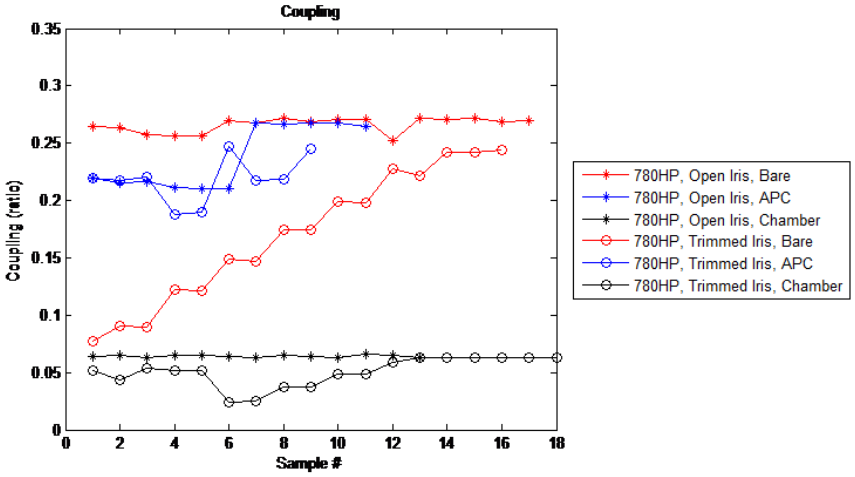

Where the x-axis, 'Sample,' refers to a specific measurement which may be separated from the others by experiment and trial. By making use of the measurements of P_{IN} and P_{OUT}, we can calculate the coupled optical power into the fibre as approximately:

$$Coupling = \frac{P_{OUT}}{0.96 P_{IN}} \tag{3.1}$$

Where the factor of 0.96 arises from the approximation of a 4% reflection at the distal cleaved end. This information is shown plotted in Figure 3.3, for both the trimmed and open iris cases of all the proximal ends for 780HP. Here, it is visible that there are no significant

differences for the APC and chamber cases, except where the power has purposely been trimmed to different levels. Additionally, the different trim settings for the flat cleave is obvious.

Figure 3.4: Average coupling for 780HP fibre for all cases.

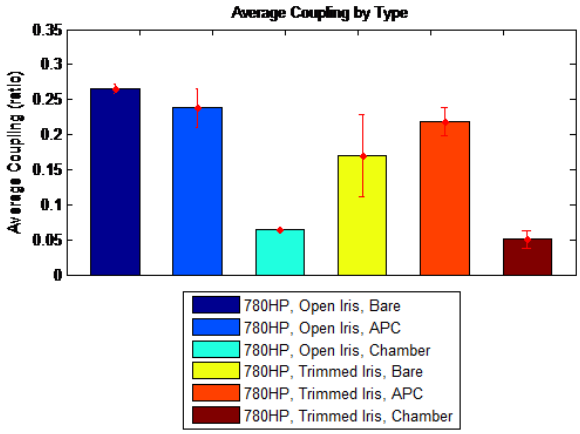

A more relevant demonstration however is arrived at by plotting the average of these values in bar format (Figure 3.4). Here the errorbars are derived from multiple experiments. Now we see quite clearly that overall, the chamber has a significantly worse coupling efficiency than either of the cleave facet or APC, which is to be expected. However, only the bare facet seems to be significantly affected by trimming the iris down. These results are unsurprising given the geometric analysis of the previous chapter. To consider the power in the signal, first consider the output power:

Figure 3.5: Output power by case, 780HP.

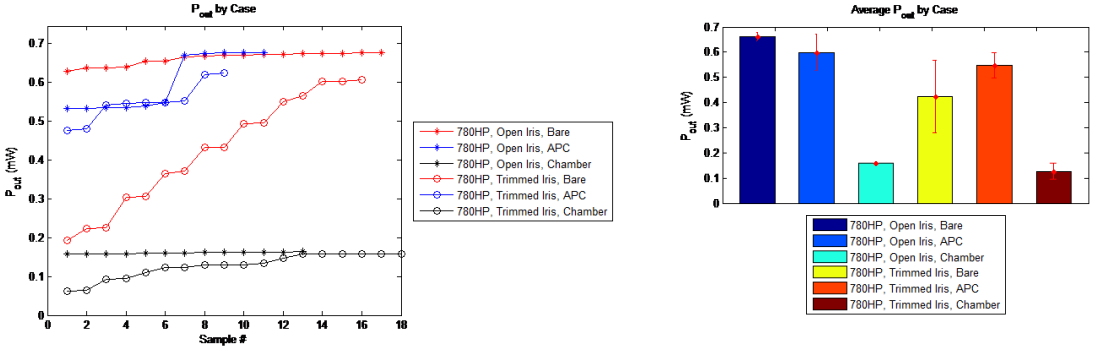

(a) (b)

Given the relationship between coupling and output power ($P_{out} = P_{OUT}$), the correlation between the plots of P_{out} by case (Figure 3.5a) and coupling (Figure 3.5b) is equally unsurprising: again, the chamber has the lowest throughput of energy. By using the measurements of P_{DET} taken when the distal end was immersed in index matching fluid as a baseline where there is negligible signal power (just background power), and measurements of P_{DET} where the end was a cleave as signal plus background, we can derive the actual quantity of signal power P_{sig} as such:

$$P_{sig} = P_{E,cleav} - P_{E,IMF} \tag{3.2}$$

Additionally, we can also calculate an approximate theoretical maximum signal power based on output power as

$$P_{sig,max} 0.5 \times 0.0396 \times P_o ut \tag{3.3}$$

Where a 50/50 split on the beamsplitter has been assumed. In reality, this appears to be

somewhat closer to a 55:45 ratio, but this is not of serious consequence for our purposes unless there is wild disagreement between the two values.

Figure 3.6: Feedback signal power by case, 780HP.

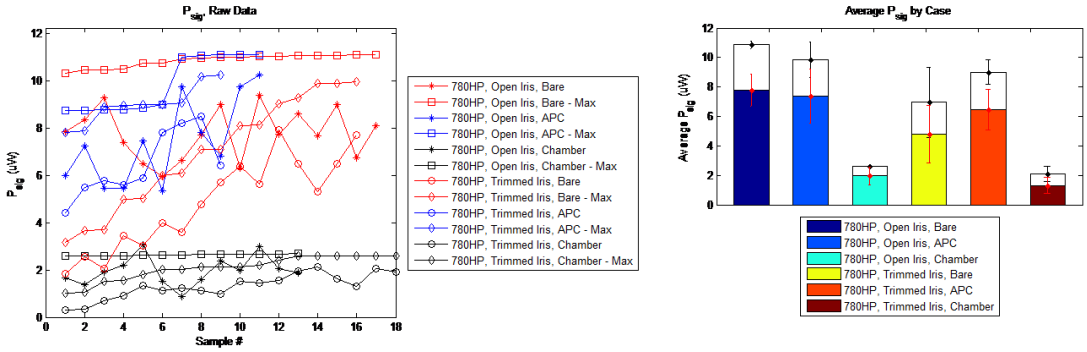

(a) (b)

Thus Figure 3.6a shows a plot of the signal power for each data point versus the calculated maximum signal power based on output. In all cases the actual signal power does not exceed this projected maximum and so in general there is good agreement. However, notable in the data is that both the cleaved facet and APC cases are generally much further below their expected maximum values than the chamber is. This is explainable because our simplistic model does not take certain efficiencies into account and assumes an optimal 4% reflection.

Figure 3.7: Feedback signal power plotted against output power, all cases, 780HP.

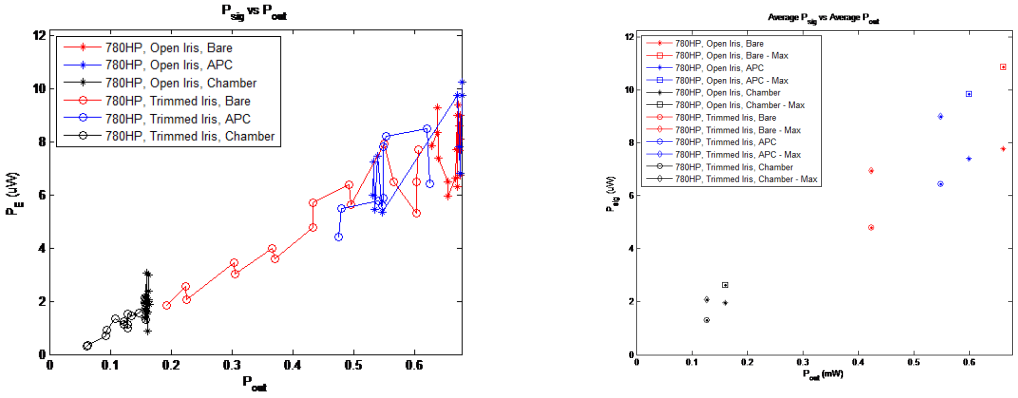

(a) (b)

If we consider signal power as a function of output power, we can then also calculate the signal power normalized by output power (Figure 3.7a). While the graph is highly suggestive of a linear relationship between the two, this becomes far more obvious in the plot of the averages (Figure 3.7b). This suggests a trend, and the slope of this should be the linear relationship of the signal power to output power in this case, a line of best fit indicates an that approximately 3.26% of the output power reflection from the tip of the fibre, which is a good fit to the expected 3.96% (approximately 17% difference).

We next consider the background power due to proximal reflection ($P_{BG,R}$) in each case. This value is derived from measurements when the distal end is immersed in IMF and normalizing these by typical values of noise. Figure 3.8a show the raw data of $P_{BG,R}$ for each data point. For one, we can see clearly that for the open iris cases, the bare fibre indeed has the highest $P_{BG,R}$, followed by APC and the chamber, respectively. In the trimmed cases, the $P_{BG,R}$ is by and large directly related to the trim level of the iris; from Figure 3.8b, which plots $P_{BG,R}$ against output power P_{OUT}, this is indeed the case.

Figure 3.9: Average background power (reflected off proximal face), all cases, 780HP

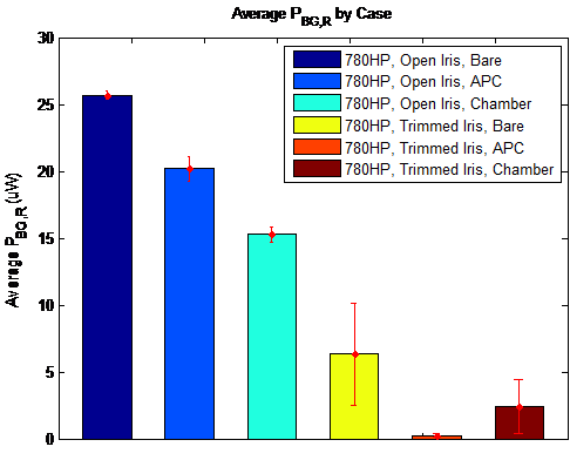

Figure 3.8: Background power (reflected off proximal face), all cases, 780HP.

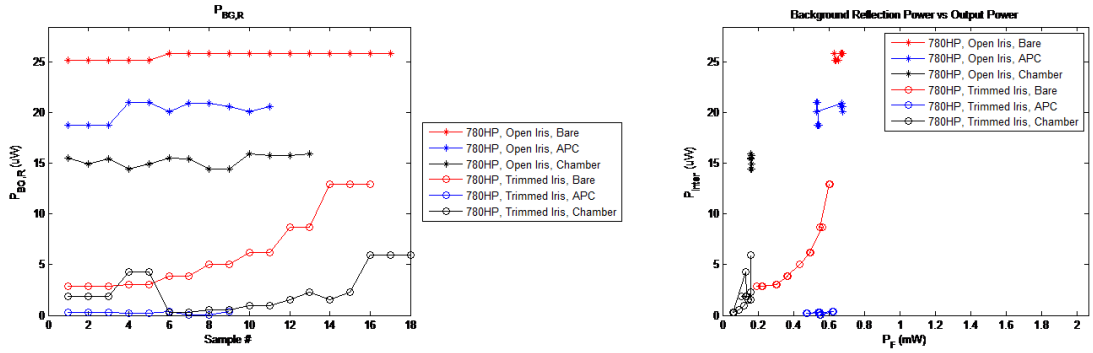

(a) (b)

If we consider the average $P_{BG,R}$ values as in Figure 3.9, below, the trend in the previous figures then becomes obvious: the intrinsic $P_{BG,R}$ is highest for bare facet (as expected) and lowest for the chamber. When an iris is utilized to trim out some of the reflection, while there is improvement across all cases, the most notable are the chamber and APC cases. Note, as well, that due to the presence of several trim levels for the cleave and chamber, these two averages are not entirely representative (which is also seen in the error bars).

Thus, because both background (interference) power and signal power are related output

power, and therefore coupling, there should be a relationship between them. Actually, they are both related to injected power, but inversely: the relative strength between them will be determined by coupling.

Figure 3.10: Background power (reflected off proximal) by feedback signal power, all cases, 780HP.

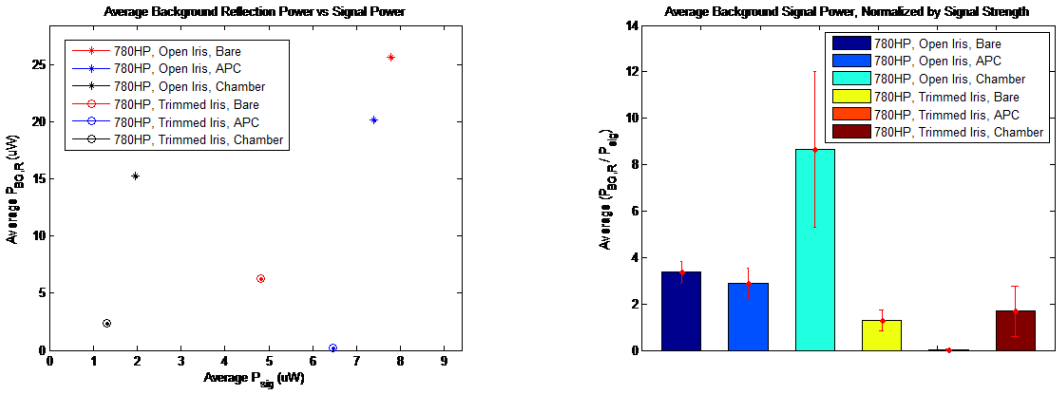

(a) (b)

From Figure 3.10, we can see that, specifically for the open iris case, despite having the highest average signal power, the flat cleave fibres have the highest $P_{BG,R}$: APC fibers have a much lower intrinsic background reflection power, and the chamber in fact has an even better one. However, when we consider the ratio between signal power to $P_{BG,R}$, we see that the chamber in fact has the worst performance. When an iris is used to trim out $P_{BG,R}$, the chamber's expected performance is still only potentially as good as a bare fibre, while the APC fibre effectively has no considerable level of $P_{BG,R}$. This is where the effect of the astigmatism on the coupling and therefore the performance of the chamber becomes clear.

Figure 3.11: Average Signal-to-Background Contrast Ratio (SBCR) for 780HP fibre for all cases.

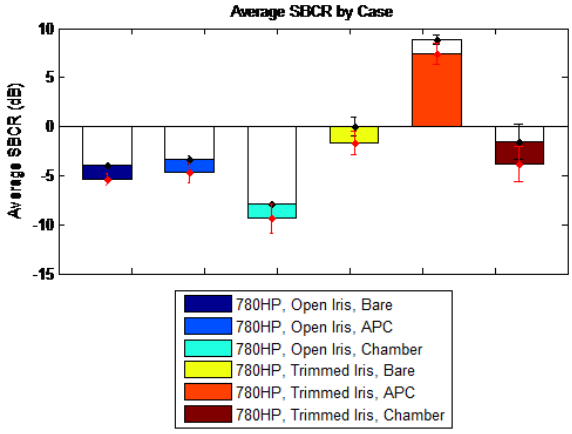

The SBCR can be calculated as:

$$SBCR = 10 \log \left(\frac{P_{sig}}{P_{BG,R}} \right) \tag{3.4}$$

The average of these is shown plotted in Figure 3.11. The coloured bars indicate the actual value of SBCR for a given case; the white bars represent the theoretical maximum as calculated using the average of $P_{sig,max}$, and the red and black errorbars are for the actual and theoretical maximum values, respectively. From this, we can clearly see that even though the chamber successfully mitigates the issue of power being reflected off the proximal end of the fibre and captured by the detector, the resulting detriment to the coupling and by logical extension, signal power, completely offsets this advantage: the performance of the chamber with no iris is actually worse than just a flat cleave, and when using an iris to trim it down, only approximately matches the performance of a flat cleave.

The theoretical maximum SBCR of a flat cleave is around 0dB; this makes sense because

the reflection should be approximately the same (4%) on both the proximal and distal ends. For a decent coupling efficiency (and coupling efficiency is generally improved when using a filtering iris), the respective power resulting from reflection on the proximal end (background) and distal end (signal) will be close to equal, thus 0dB.

Finally, we note first that the APC fibre has a similar SBCR to the flat cleave for the open iris case. This is because the typical cleave angle of APC fibre, 8 deg, is not enough to cause the reflection to fall outside the collection angle of the objective. However, when the iris is trimmed down, the reflection is blocked from the objective without sacrificing actual power coupled into the APC fibre in fact, for some trim settings, improving it. This can essentially be summarized as the flat cleaved fibre has the benefit of good coupling and therefore strong signal power; the chamber has the benefit of low reflection (background) power; and the APC combines both of these aspects. As a result, not only does it have the best performance when used in conjunction with an iris, but it is the only case that had a SBCR greater than 0dB, with the average SBCR at approximately 7.4dB. Considering that an AR coating that reduces the reflectance by a factor of 4 will only improve this to approximately 6dB, the results here have proven effectively superior to the complication and expense of AR coating and represent a wide-band solution.

Realizing then from equation 3.4 that SBCR can be improved either by increasing P_{sig} or decreasing P_{BG}, there should be an obvious correlation between P_{sig} and SBCR. Indeed, by graphing the SBCR against signal power level for various cases shows this is the case (Figure 3.12).

Figure 3.12: Signal-to-Background Contrast Ratio (SBCR) vs Signal Power for 780HP fibre for all cases.

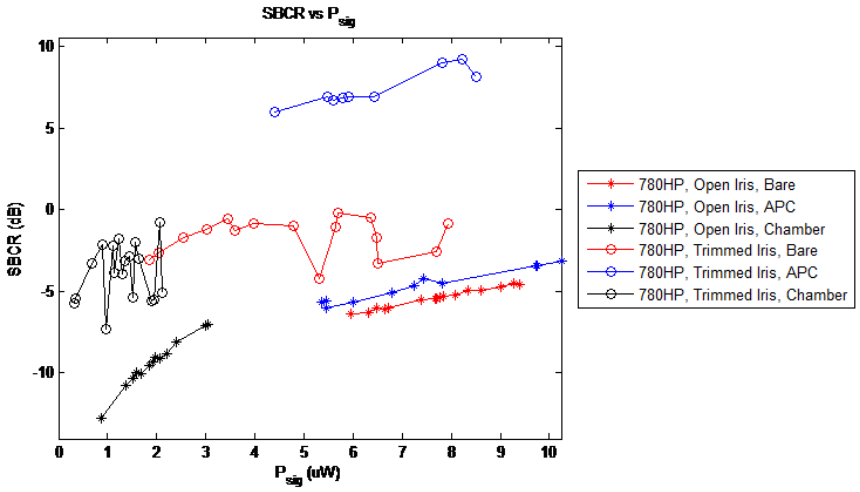

Specifically, Figure 3.12 shows that within a specific test case, there is a general improvement of SBCR as signal level increases. However, mileage seems to vary; in some cases, such as the open-iris chamber case, a marginal improvement of signal power results in a very significant change in SBCR, whereas for the open-iris APC and flat cleave cases, there is only minimal improvement by comparison. This can be understood as the chamber having intrinsically low background reflection power, and therefore the dominant factor becomes signal power; whereas the APC and cleave cases are swamped by background power and so even a two-fold improvement in signal power does little in the way of improvement. Clearly, both factors must be considered, which is why the iris-trimmed APC case dominates in terms of performance.

Our general analysis now done, we consider the total results from all fibres to see what role the degree of multimodality plays.

3.3.1 Discussion of Other Fibre Types

We have investigated in detail the results and analysis of 780HP optical fibre - a synonymous procedure for the other 3 types of ibre was performed and likewise results summarized and analyzed. These are available in Appendix A and will be discussed here.

In the case of SM600, at the given wavelength, the fibre should be single-mode. We see that primarily the results do not diverge much from the 780HP case, except that overall SBCR is lower in most cases. This is related to the fact that the signal power (and therefore coupling) is lower as coupling light to a single-mode fibre is more difficult and also highly dependent on perfect alignment. Especially in the case of the chamber, distortion of the input field prevents effectively coupling into the fibre, marring results.

These differences are ameloriated in the 980-5.8-125 fibre case, in fact, the coupling was generally the best of all fibres; even the trimmed flat cleave case has an SBCR over 0, though once again the chamber has a much lower SBCR and results overall agree with what has so far been observed.

Finally, SMF28e+ has likewise typical results, but most notably, it continues the trend of chamber performance improving with increased V number. All fibres compared with each other will now be considered.

3.3.2 Comparison of Fibre Types

Figure 3.13: Comparison of All Fibre Types for Proximal Flat Cleave Case

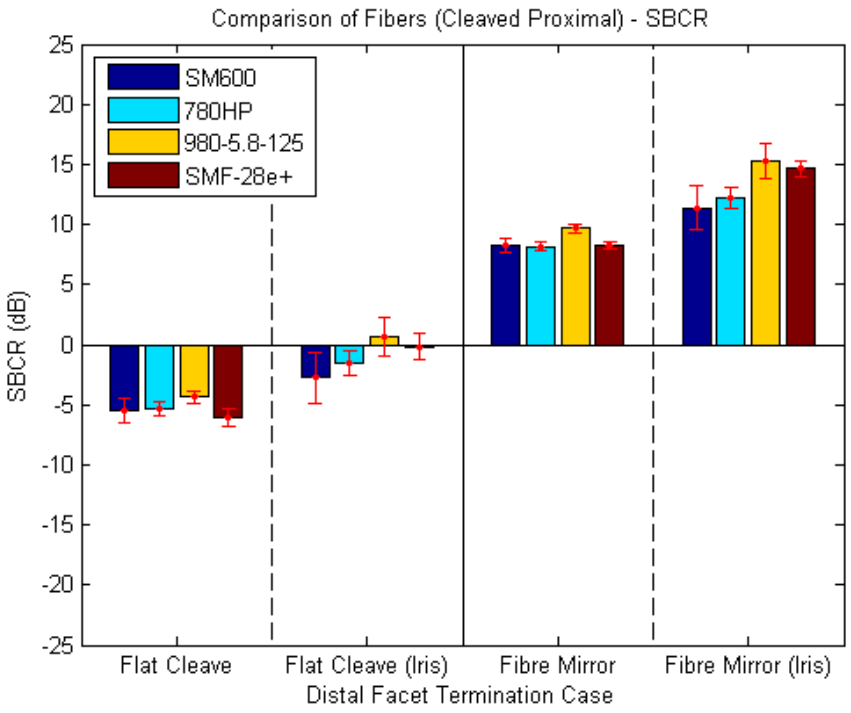

Figure 3.13 shows the collective results for the four different types of fibre for the cleaved facet proximal case. While some minor differences exist, when an iris is not used, in general the average SBCR is the same for all cases, approximately -6dB. Notably, there is a slight difference for the 980-5.8-125 case. When an iris is used to trim out the reflection power, we see that there is indeed a slight, but notable difference between the cases, and in general, the SBCR improves as the V number increases. Data is also provided for fibre mirrors of each type, which will have SBCRs 14dB higher than their respective bare facet cases if our data is reliable; this appears to hold valid in all cases thus providing a level of validation. Additionally, it also appears to validate the slightly better SBCR value for the open-iris 980-5.8-125 fibre as well as the differing levels for the trimmed case as their relative levels

are in agreement.

From a coupling standpoint, this makes sense. For a single mode fibre, coupling efficiency is highly dependent on the overlap of the incident power with the fundamental mode of the fibre at that wavelength: therefore, not only does it need the same, approximately Gaussian shape, but it must also be scaled properly to couple efficiently. However, as V number increases and therefore additional modes can propagate, coupling becomes more efficient. For a few-mode fibre, this can be understood that light will couple into higher-order modes that share a non-zero overlap integral with the incident power; therefore, even light that does not successfully couple into the fundamental mode may couple into these additional modes that are not available in the single-mode fibre. For very multimode fibres, this essentially becomes a matter of matching the numerical apertures of the fibre and coupling lens. Therefore, because more of the incident energy is able to couple into fibres with higher V-numbers, less will be lost or reflected, suggesting a better SBCR level. As for why this occurs only when an iris is used to trim, this could simply be a matter of when the iris is open, the signal, regardless of minute differences, is buried.

Figure 3.14: Comparison of All Fibre Types for Proximal APC Case

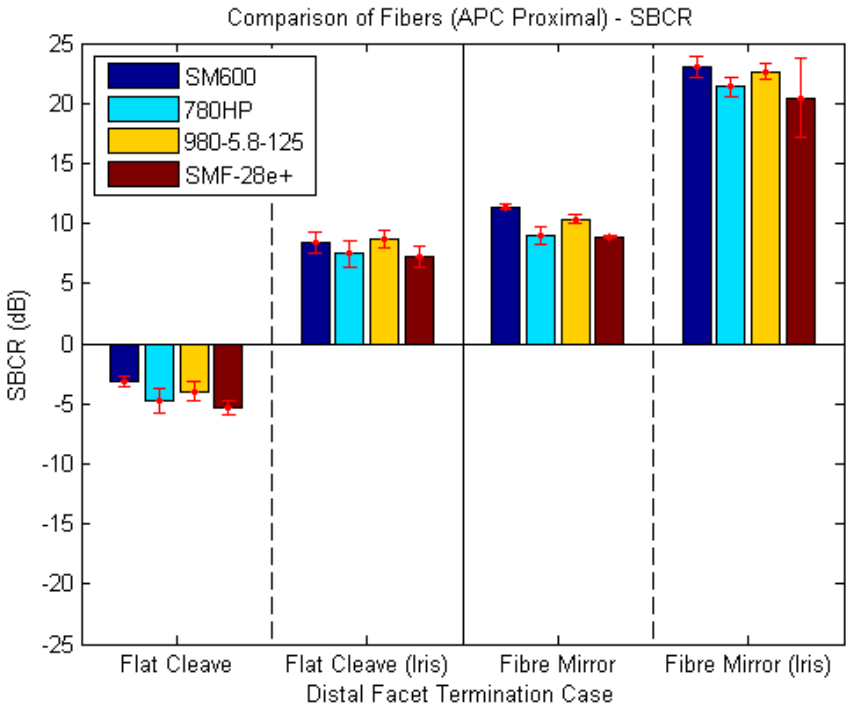

Figure 3.14 shows the results for each fibre type for the APC case. We note that these results fulfill our expectations from the previous analysis, in that for the open iris case, the SBCR levels are similar to those of the flat proximal cleave; however, when an iris is used, there is significant improvement. In this case however, although the 980-5.8-125 still has notably elevated levels, so does the SM600. In reality, this could be for a variety of reasons; notably, that there is a variation in the type of fibre used for the flat cleave versus the APC fibre (though both are Thorlabs SM600, some coupling differences were noted suggesting different properties, perhaps due to manufacturing variation). Additionally, SM600 is single-mode, and it is possible that the holder for the APC ferrule was more stable and therefore had better alignment. In the end, the variation is only a few decibels and therefore not of major significance. Again, fibre mirror results validate our results.

Figure 3.15: Comparison of All Fibre Types for Proximal APC Case

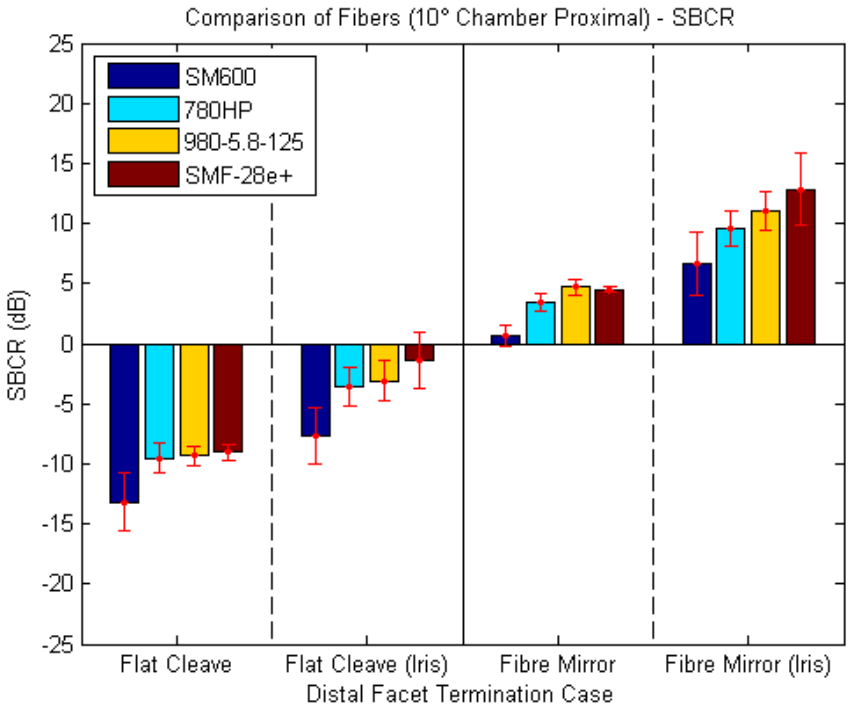

Figure 3.15 shows the results for the chamber for all fibre types, and clearly demonstrates the greatest level of variation between fibre types. Contrary to APC, the single-mode SM600 fibre actually has the worst SBCR for both the open-iris and trimmed-iris cases. As well, though the variations are much smaller for the open-iris case, they are far more evident in the trimmed-iris case, and it is clear that SBCR improves for fibres with higher V-numbers. This is again validated by the fibre mirror results. This also meshes very well with the explanation offered previously: the astigmatism becomes less of an issue for multimode fibres. For the single-mode SM600, the distortion of the input signal seriously inhibits efficiency coupling, because the originally Gaussian-shaped input signal is altered, reducing overlap with the fundamental mode. For the fibres with much higher V-numbers, like SMF28e+, this is not an issue, because the incident light will likely couple as long as it is within the acceptance

cone defined by the fibre's NA.

3.3.3 Comparison of APC and Chamber

So far we have seen then that the SBCR levels are dependent on both good coupling and low background reflection, rather than just one or the other. As a fibre's coupling should generally improve with increased V number, the SBCR will also increase as V number does. We return to a conjecture made at the end of the previous chapter: that the APC fibre is simply a limiting case of the chamber's method of action. One way to potentially prove that this is true and that therefore the difference in SBCR levels is purely based on deficiencies in coupling is to decouple the APC fibre until its output power matches that of the respective chamber case.

Figure 3.16: Comparison of APC and Chamber Results for Same Output Power, 780HP.

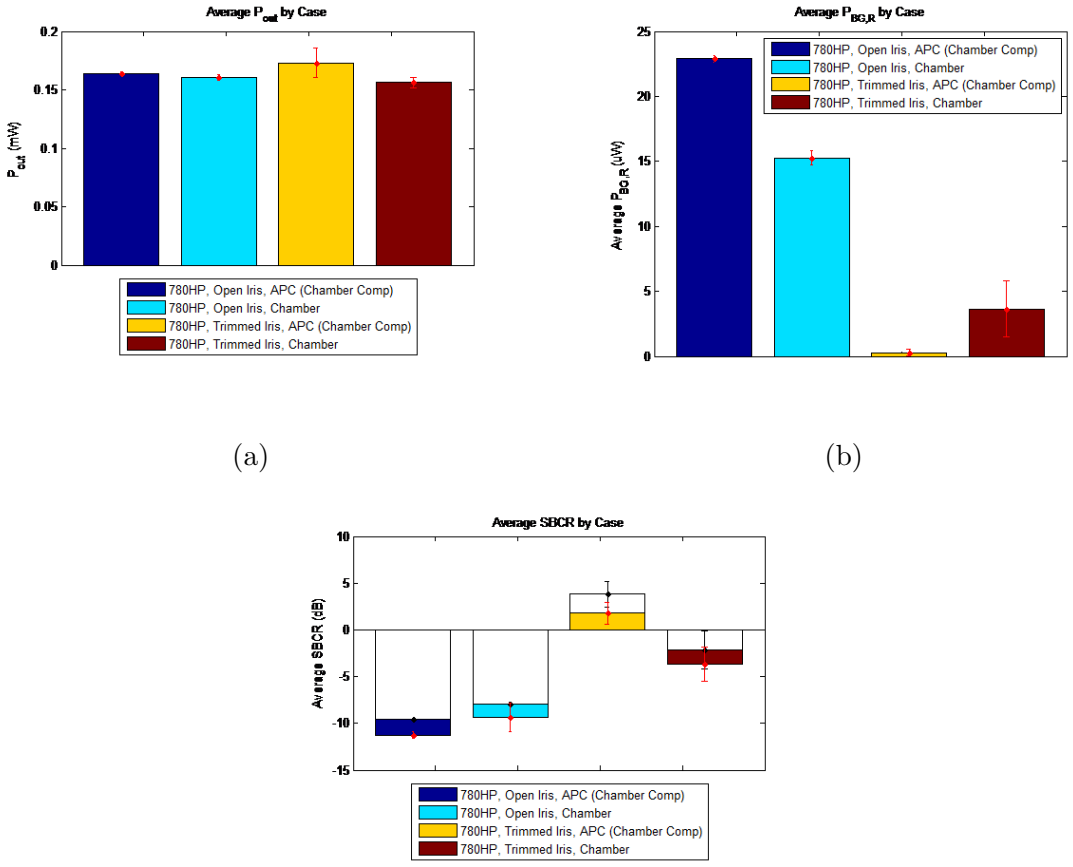

Figure 3.16a shows the average output power for the chamber cases as well as two special APC cases where the fibre has been purposely detuned to the same coupling levels. However, importantly, for the chamber, trimming the iris reduced the output power P_{OUT}, whereas (strangely) for the APC fibre, it increased it. This increase is minimal approximately 5-6% - but still notable and possibly due to constructive or destructive interference effects improving mode overlap.

Next, examining the proximal reflection powers as in Figure 3.16b, we see that even though the APC fibre has a much higher $P_{BG,R}$, it drops to negligible levels when trimmed with an iris. Presumably, then, because the output powers P_{OUT} are so similar, the signal power

P_{sig} can be assumed to also be similar. Then, given the $P_{BG,R}$ levels above and assuming minimal variation for intrinsic system background noise (that is, from other components) , we would expect the chamber to have a superior SBCR for the open iris case and the APC fibre to have a better SBCR when an iris is used to trim out the reflection.

Plotting the average SBCR levels (Figure 3.16c), we see this is exactly the case. Then, we can draw a few conclusions from this comparison. For one, when we equalized the output power P_{OUT} of the chamber and APC cases, the SBCR levels became much more similar. The limiting factor then is the reflected background power, $P_{BG,R}$. As to why they differ, this is again a matter of geometry: the APC fibre face is at approximately 8 deg while the chamber face is at approximately 14.7 deg. Therefore, in the case of a fully open iris, the light reflected off the face of the APC fibre will have more overlap with the acceptance area of the objective; in fact, it will be almost completely within it. Meanwhile, the chamber, with the greater incidence angle, will not have all of its reflected light collected by the objective. However, when the iris is closed, because the light will be focused on the face of the APC fibre, it can be completely blocked by the iris; however, the chamber window, with a much larger surface area at a much closer spacing, will still reflect some of the light back into the objective. This is also due to various other effects, such as multiple reflections between the window and IMF.

3.3.4 Comparison of Flat Cleave and FC/PC

As a final consideration, we look at similarities or differences between a flat proximal end and an FC/PC grind.

Figure 3.17: Comparison of FC/PC and Flat Cleave Results, SM600.

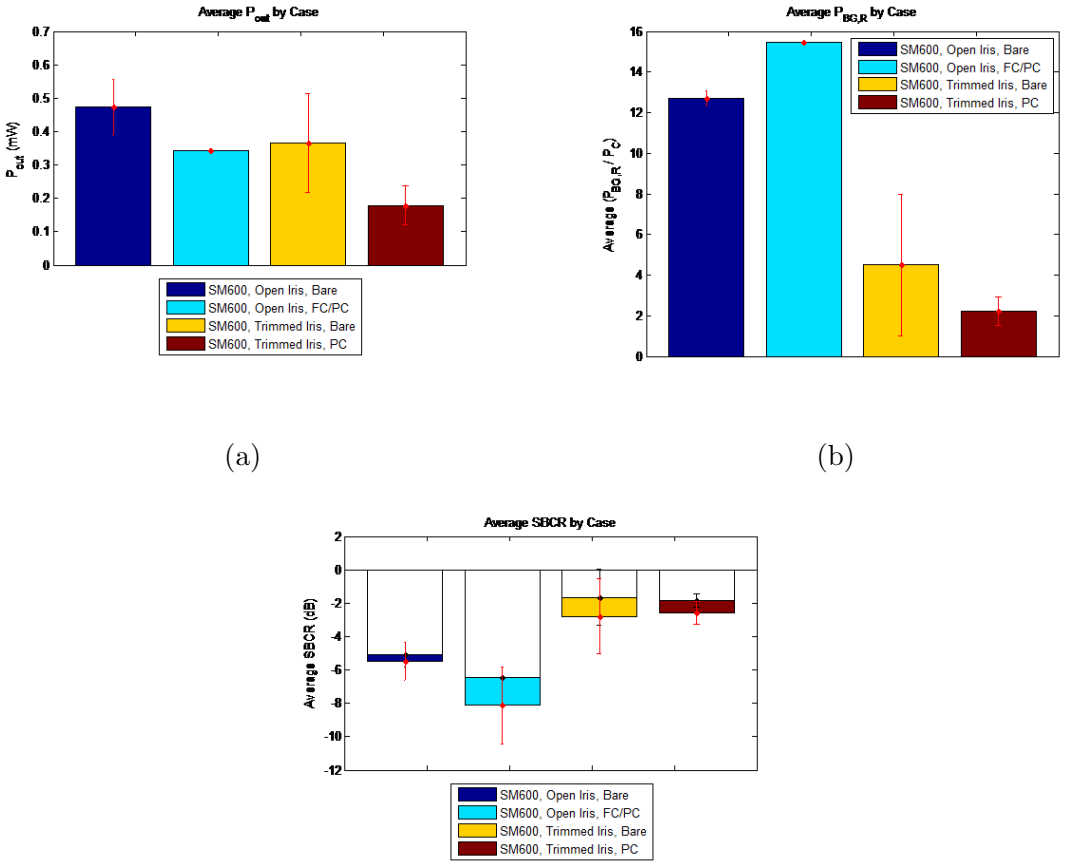

(a) (b)

(c)

Figure 3.17 shows that in general, a flat cleave has better output power P_{OUT}, and thereby a better coupling and higher signal power P_{sig}. However, the FC/PC cable has a higher background power $P_{BG,R}$ in the open iris case and a lower one for the trimmed iris. Given this then, it is unsurprising that they have similar SBCRs. Therefore, given the easy of create a flat cleave and the fact that its performance is superior in the open iris case, there is no utility in using an FC/PC fibre.

Chapter 4

Conclusions and Future Work

4.1 Conclusions

This work has been motivated by the drive to apply techniques of mode control in multimode fibres to distributed fibre Bragg grating sensor systems. In particular, adaptive optic techniques that began in imaging (specifically in turbid media imaging) and have been extended to overcome bandwidth limitations in optical communications (specifically mode division multiplexing, MDM) are beginning to become attractive methods by which to interrogate specific sensors in quasi- and fully-distributed systems. However, realization of such a deployment requires the ability to both calibrate the system, as well as realize full independent control of the injected power distribution. Therefore, we need to be able to freely inject an arbitrary pattern into the entry point of such a system namely a fibre and also receive a response signal from that same fibre, with requisite fidelity of information such that we can decompose the modal content subject to a transmission matrix T.

It was found that a primary limiting factor in realizing these potentials was background optical energy that was a result of the injection of this signal itself. In order to address this issue and resolve a method by which we can simultaneously inject and extract a signal

from the same spatial point, we defined a quantity called the Signal-to-Background Contrast Ratio, SBCR. Then, we have shown that SBCR can be increased easily using only geometric optics and spatial filtering; this resulted in improvements of over 7dB have been made using only alignment and an iris. A specialized refraction chamber was constructed under these principles, and its feasibility was demonstrated. Experimentation further found that the use of an FC/APC grind is the superior case, and in conjunction with an iris to trim the unwanted proximal reflection, was able to essentially completely eliminate it. Performance is based on signal power (therefore coupling) as well as mitigating this unwanted reflection: this was shown to be the sole limiting factor on the chamber design. Additionally, multimode fibres have inherently better coupling, meaning SBCR improves with increasing V number. All of this has been done without resorting to more costly and complicated methods such as depositing anti-reflection coatings.

4.2 Future Work

Regardless, this has not been an exhaustive work, and several cases and avenues remain to be explored. For instance, an actual test of this system with an adaptive optics setup, utilizing either a spatial light modulator (SLM) or deformable mirror (DM) is a vital next step in developing such a system. Primarily, an excellent proof-of-concept would be the characterization of the transmission matrix T of a given fibre using reflection-only based measurements. This would help to prove the fidelity of the modal information in the signal, especially for highly multimodal fibres. Following this, arbitrary mode control is then feasible and demonstrable, and an actual test with an FBG sensor system is possible.

Regarding the refraction chamber design itself, despite the fact that for the arbitrary case of a static, injected signal, it was shown that the FC/APC fibre face has more attractive properties, there are still areas left to be explored. The chamber offers several distinct advantages: for one, the chamber is a universal solution for any step-index fibre provided

that an index matching solution can be found or fabricated for it. It is inexpensive, quick to fabricate, and easy to replace a damaged fibre whereas FC/APC fibres may not be available for a given fibre type, are more expensive, or are time consuming to produce. Finally, it offers the advantage of having the origin of the reflection power being spatially separated from the origin of the signal of interest (the fibre face).

Several cases still remain to be considering for the chamber design: for one, the fibre in the chamber was held at a statistically fixed distance from the front window. Different spacings, especially ones where the fibre face is much close to the front of the window, could prove to have significant improvements in SBCR. Additionally, there are front window designs themselves that could significantly improve chamber performance: for instance, a window that is ground to different thicknesses (and has a different index of refraction than the IMF filling the chamber) could help to overcome the astigmatic effects described in Chapter 2. Other methods that are standard in the field of optic design for overcoming astigmatism in lenses could also be used, as could GRIN lenses. Finally, an investigation into the use of anti-reflection coatings on the window face could offer insight to further improvements in its utilization.

As for the conclusion that a simple FC/APC interface provides improvements that even surpass a high-quality AR coating, there is still room for improvement. As the proximal reflection power in this case has been almost entirely eliminated, the SBCR is then dominated by the signal power. Short of increasing the injected power or somehow otherwise improving coupling, other methods, such as amplified detectors or more sensitive detectors could be used.

In finality, these results are relevant to any case that utilizes mode division multiplexing or requires access to the modal information, such as fibre characterization, imaging (especially turbid media imaging), or other multimode communications or sensor deployments, meaning that the results here are not just limited to a narrow scope such as the intended system of deployment described herein. Instead, the ability to access and characterize multimode fibres

is an important result for most major fields involving fibre optics.

Bibliography

[1] AW Snyder and J Love. *Optical Waveguide Theory*. Chapman & Hall, 1 edition, 1983.

[2] Amonon Yariv and Pochi Yeh. *Photonics: Optical Electronics in Modern Communication*. The Oxford Seres in Electrical and Computer Engineering. Oxford University Press, 6 edition, 2006.

[3] Gard Keiser. *Optical Fiber Communications*. McGraw-Hill Science/Engineering/Math, 4 edition, 2010.

[4] R. Essiambre and R.W. Tkach. Capacity trends and limits of optical communication networks. *Proceedings of the IEEE*, 100(5):1035–1055, May 2012.

[5] D. J. Richardson, J. M. Fini, and L. E. Nelson. Space-division multiplexing in optical fibres. *Nature Photonics*, 7(5):354–362, 05 2013.

[6] S. Berdagué and P. Facq. Mode division multiplexing in optical fibers. *Appl. Opt.*, 21(11):1950–1955, Jun 1982.

[7] R. Ryf, S. Randel, A.H. Gnauck, C. Bolle, A. Sierra, S. Mumtaz, M. Esmaeelpour, E.C. Burrows, R. Essiambre, P.J. Winzer, D.W. Peckham, A.H. McCurdy, and R. Lingle. Mode-division multiplexing over 96 km of few-mode fiber using coherent 6x6 mimo processing. *Lightwave Technology, Journal of*, 30(4):521–531, Feb 2012.

[8] Fumiya Saitoh, Kunimasa Saitoh, and Masanori Koshiba. A design method of a fiber-based mode multi/demultiplexer for mode-division multiplexing. *Opt. Express*, 18(5):4709–4716, Mar 2010.

[9] Massimiliano Salsi, Clemens Koebele, D. Sperti, P. Tran, H. Mardoyan, P. Brindel, S. Bigo, A. Boutin, F. Verluise, Pierre Sillard, M. Astruc, L. Provost, and Gabriel Charlet. Mode-division multiplexing of 2x100 gb/s channels using an lcos-based spatial modulator. *Lightwave Technology, Journal of*, 30(4):618–623, Feb 2012.

[10] Kai Shi, G.S.D. Gordon, and B.C. Thomsen. Degenerate mode-group division multiplexing using delayed adaptive frequency-domain equalization. In *Optical Fiber Communications Conference and Exhibition (OFC), 2014*, pages 1–3, March 2014.

[11] Neng Bai, Ezra Ip, Yue-Kai Huang, Eduardo Mateo, Fatih Yaman, Ming-Jun Li, Scott Bickham, Sergey Ten, Jesús Li nares, Carlos Montero, Vicente Moreno, Xesús Prieto, Vincent Tse, Kit Man Chung, Alan Pak Tao Lau, Hwa-Yaw Tam, Chao Lu, Yanhua Luo, Gang-Ding Peng, Guifang Li, and Ting Wang. Mode-division multiplexed transmission with inline few-mode fiber amplifier. *Opt. Express*, 20(3):2668–2680, Jan 2012.

[12] M. Kasahara, K. Saitoh, T. Sakamoto, N. Hanzawa, T. Matsui, K. Tsujikawa, F. Yamamoto, and M. Koshiba. Design of few-mode fibers for mode-division multiplexing transmission. *Photonics Journal, IEEE*, 5(6):7201207–7201207, Dec 2013.

[13] Hirokazu Kubota and Toshio Morioka. Few-mode optical fiber for mode-division multiplexing. *Optical Fiber Technology*, 17(5):490 – 494, 2011. 100G and Beyond.

[14] Neng Bai, Ezra Ip, Ting Wang, and Guifang Li. Multimode fiber amplifier with tunable modal gain using a reconfigurable multimode pump. *Opt. Express*, 19(17):16601–16611, Aug 2011.

[15] J. Carpenter, B.C. Thomsen, and T.D. Wilkinson. Degenerate mode-group division multiplexing. *Lightwave Technology, Journal of*, 30(24):3946–3952, Dec 2012.

[16] D. Gloge. Weakly guiding fibers. *Appl. Opt.*, 10(10):2252–2258, Oct 1971.

[17] L. Palmieri and A. Galtarossa. Coupling effects among degenerate modes in multimode optical fibers. *Photonics Journal, IEEE*, 6(6):1–8, Dec 2014.

[18] N.A. Kaliteevskiy, A.E. Korolev, K.S. Koreshkov, V.N. Nazarov, and P.M. Sterlingov. Two-mode coupling model in a few mode fiber. *Optics and Spectroscopy*, 114(6):913–916, 2013.

[19] Reza Nasiri Mahalati, Daulet Askarov, Jeffrey P. Wilde, and Joseph M. Kahn. Adaptive control of input field to achieve desired output intensity profile in multimode fiber with random mode coupling. *Opt. Express*, 20(13):14321–14337, Jun 2012.

[20] I. M. Vellekoop and A. P. Mosk. Focusing coherent light through opaque strongly scattering media. *Opt. Lett.*, 32(16):2309–2311, Aug 2007.

[21] Tomáš Čižmár and Kishan Dholakia. Shaping the light transmission through a multimode optical fibre: complex transformation analysis and applications in biophotonics. *Opt. Express*, 19(20):18871–18884, Sep 2011.

[22] Ioannis N. Papadopoulos, Salma Farahi, Christophe Moser, and Demetri Psaltis. Focusing and scanning light through a multimode optical fiber using digital phase conjugation. *Opt. Express*, 20(10):10583–10590, May 2012.

[23] Joel Carpenter, Benjamin J. Eggleton, and Jochen Schröder. 110x110 optical mode transfer matrix inversion. *Opt. Express*, 22(1):96–101, Jan 2014.

[24] Eric Udd and William B. Jr Spillman. *Fiber Optic Sensors: An Introduction for Engineers and Scientists*. Wiley, 2 edition, 2011.

[25] Shiao-Min Tseng and Chin-Lin Chen. Optical fiber fabry-perot sensors. *Appl. Opt.*, 27(3):547–551, Feb 1988.

[26] A. Kersey, M.A. Davis, H.J. Patrick, M. Leblanc, K.P. Koo, C.G. Askins, M.A. Putnam, and E.J. Friebele. Fiber grating sensors. *Lightwave Technology, Journal of*, 15(8):1442–1463, Aug 1997.

[27] Yun-Jiang Rao. In-fibre bragg grating sensors. *Measurement Science and Technology*, 8(4):355, 1997.

[28] I. Baumann, J. Seifert, W. Nowak, and M. Sauer. Compact all-fiber add-drop-multiplexer using fiber bragg gratings. *Photonics Technology Letters, IEEE*, 8(10):1331–1333, Oct 1996.

[29] Hong-Gang Yu, Chun Yang, Yong Wang, Jing-Song Zhang, Jian Yang, Robert Farkas, and Chang-Qing Xu. Bragg gratings in multimode fiber. volume 5577, pages 354–361.

[30] R.A. Perez-Herrera and M. Lopez-Amo. Fiber optic sensor networks. *Optical Fiber Technology*, 19(6, Part B):689 – 699, 2013. Optical Fiber Sensors.

[31] K.T.V. Grattan and T. Sun. Fiber optic sensor technology: an overview. *Sensors and Actuators A: Physical*, 82(13):40 – 61, 2000.

[32] Ruo Yu Gu, Reza Nasiri Mahalati, and Joseph M. Kahn. Noise-reduction algorithms for optimization-based imaging through multi-mode fiber. *Opt. Express*, 22(12):15118–15132, Jun 2014.

[33] Edmund Optics. Mgf2 anti-reflection coating performance.

Appendices

Appendix A

Data for Other Fibre Cases

A.1 SM600

Figure A.1: Power Characteristics, SM600

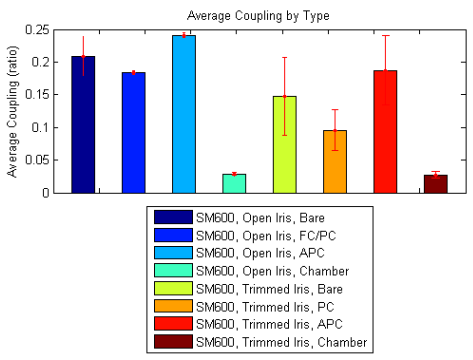

(a) Coupling

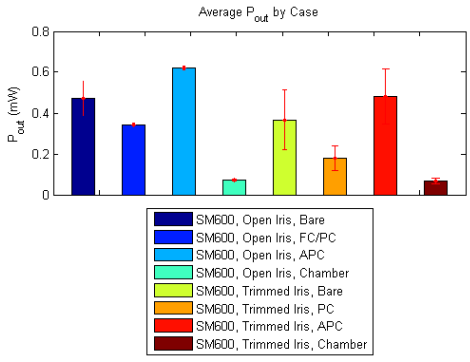

(b) Output Power

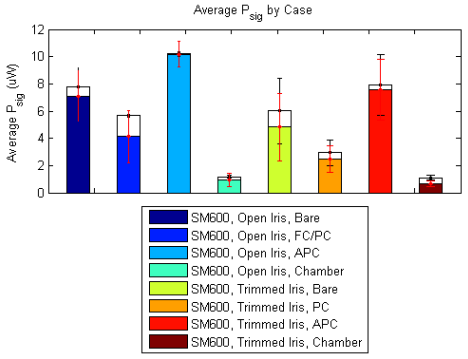

(c) Signal Power

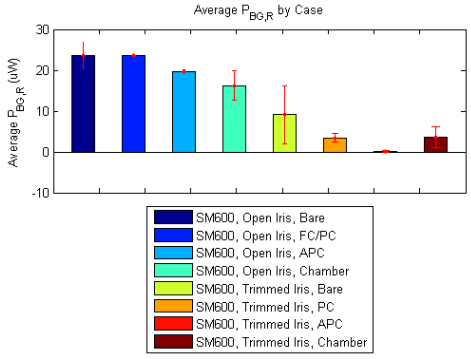

(d) Background Power

Figure A.2: Signal-to-Background Contast Ratio Data, SM600

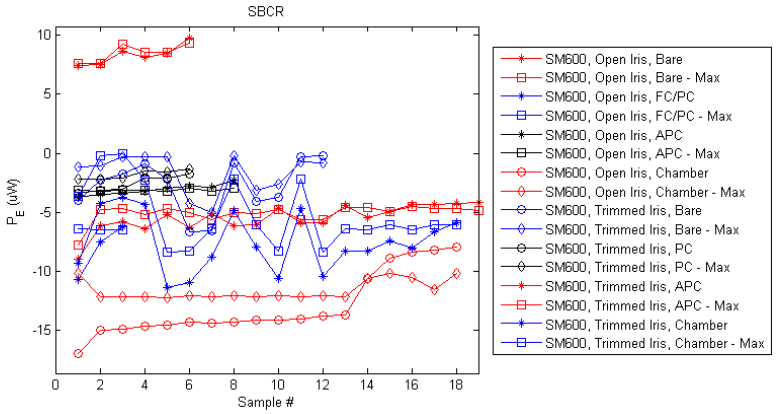

(a) Raw SBCR data

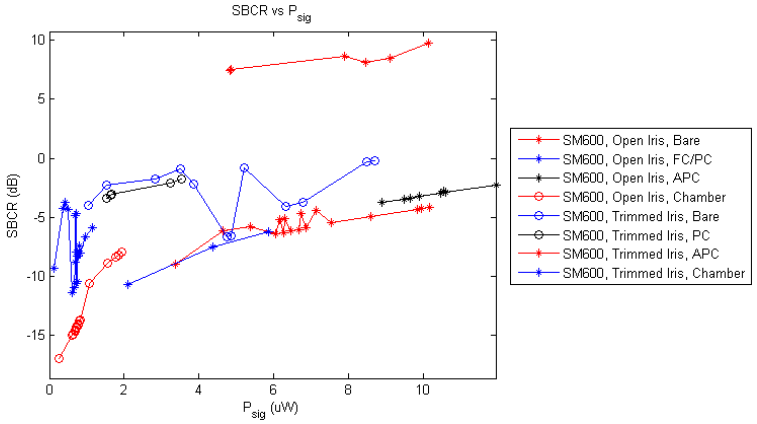

(b) SBCR vs Signal Power

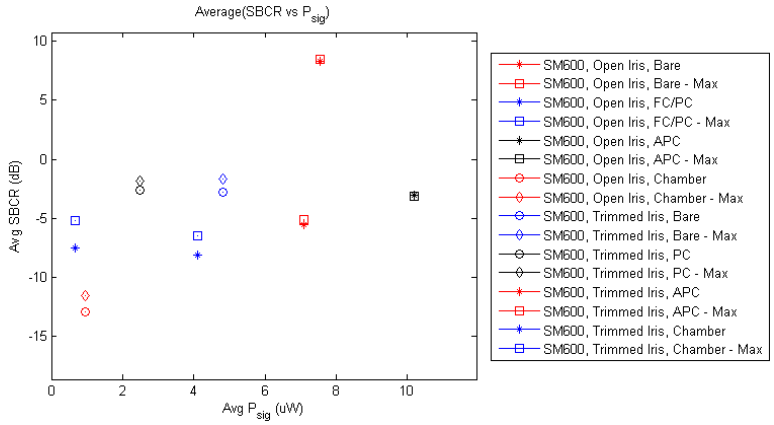

(c) Average SBCR vs Average Signal Power

Figure A.3: Average SBCR

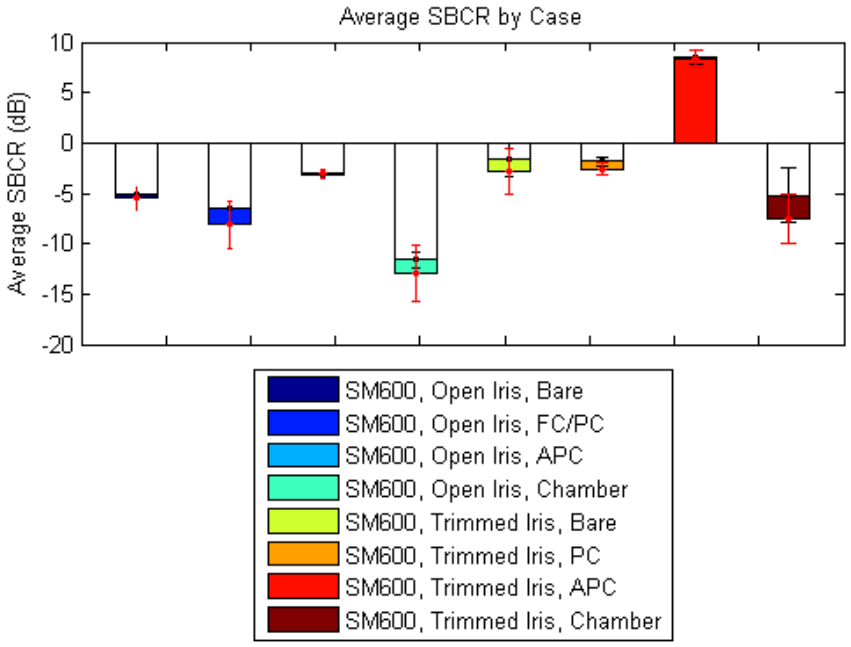

SM600 Chamber/APC Comparison

Figure A.4: Comparison of Chamber and APC Results, SM600

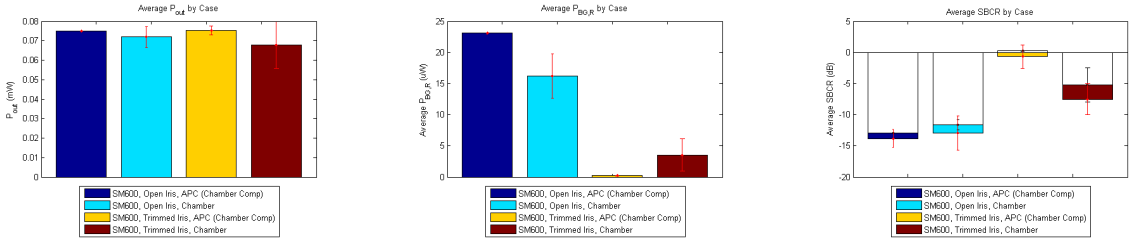

(a) (b) (c)

A.2 980-5.8-125

Figure A.5: Power Characteristics, 980-5.8-125

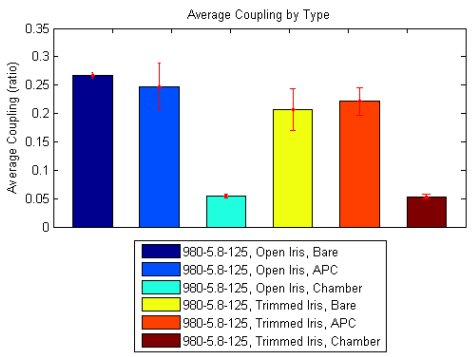

(a) Coupling

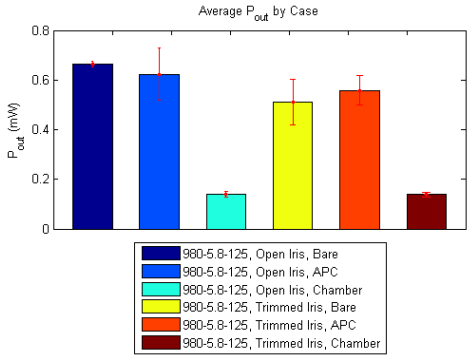

(b) Output Power

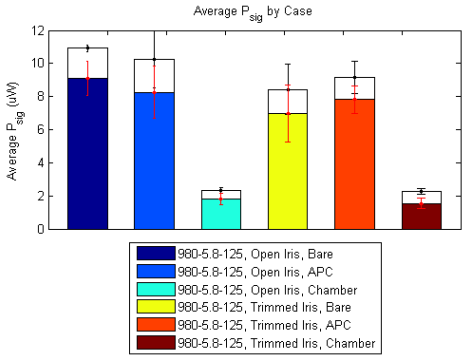

(c) Signal Power

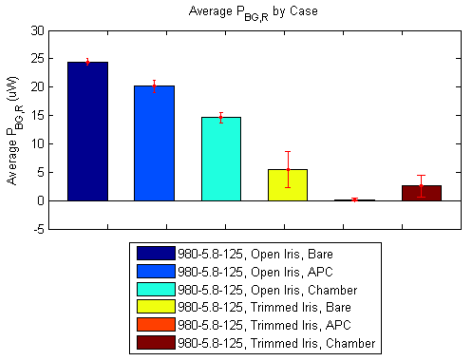

(d) Background Power

Figure A.6: Signal-to-Background Contast Ratio Data, 980-5.8-125

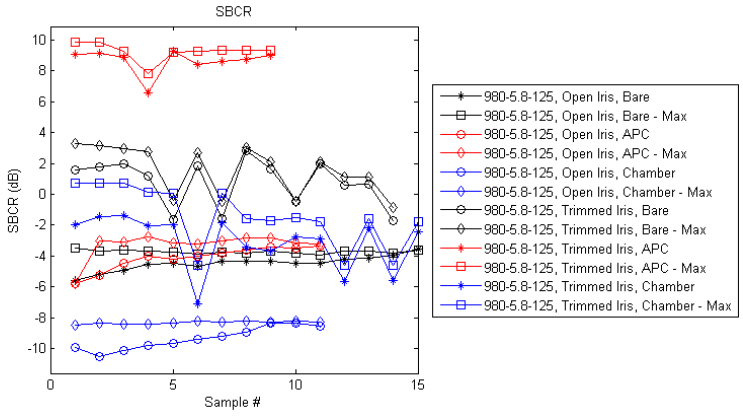

(a) Raw SBCR data

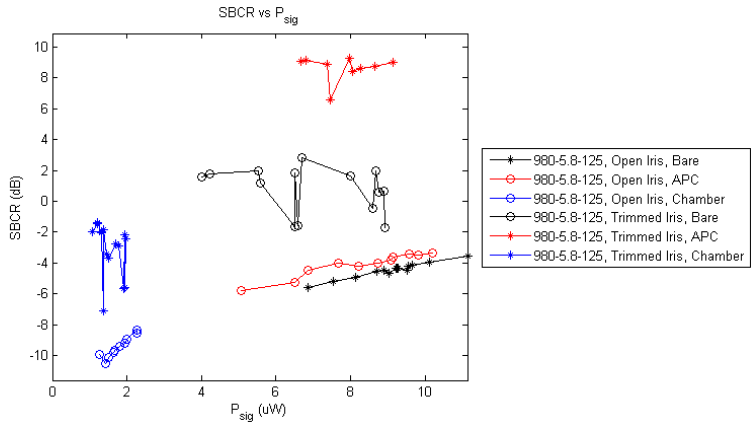

(b) SBCR vs Signal Power

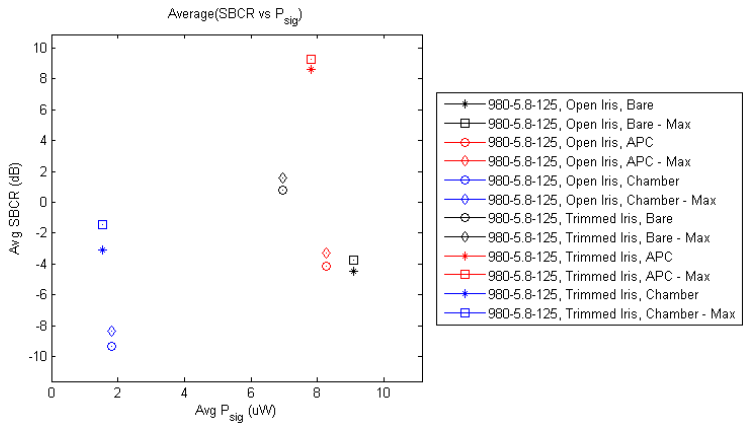

(c) Average SBCR vs Average Signal Power

Figure A.7: Average SBCR

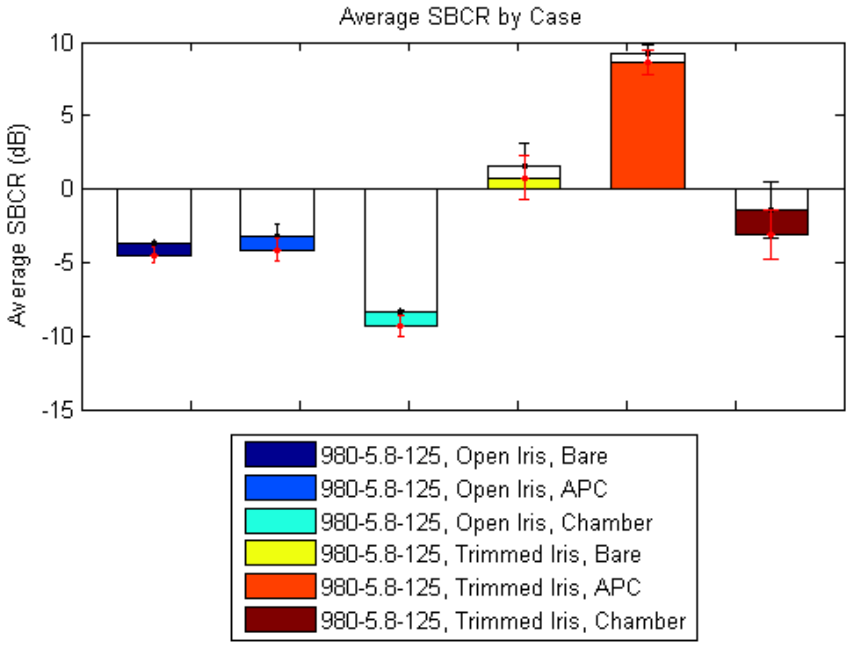

980-5.8-125 Chamber/APC Comparison

Figure A.8: Comparison of Chamber and APC Results, 980-5.8-125

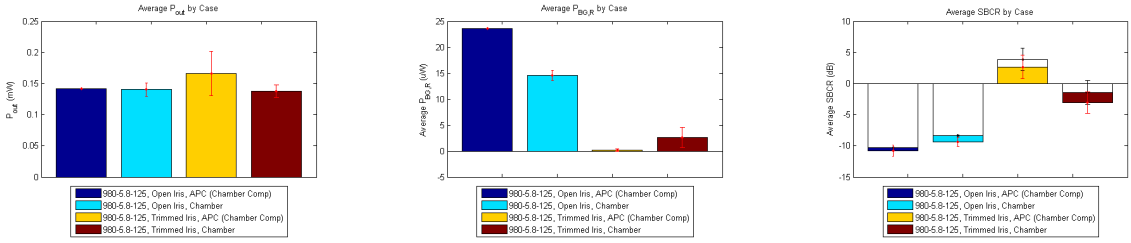

(a) (b) (c)

A.3 SMF-28e+

Figure A.9: Power Characteristics, SMF28e+

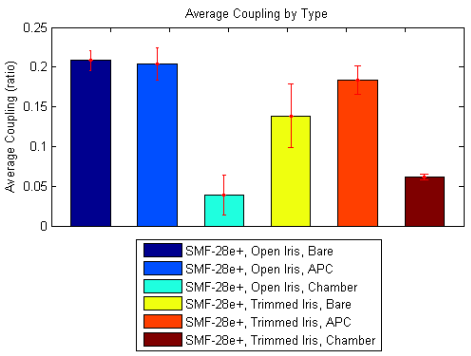

(a) Coupling

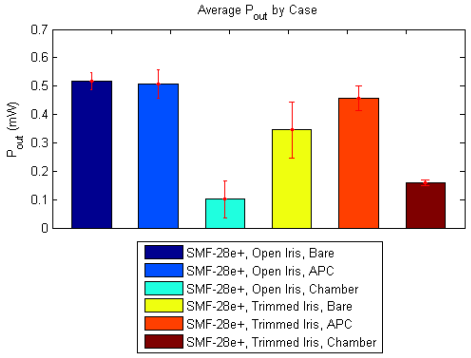

(b) Output Power

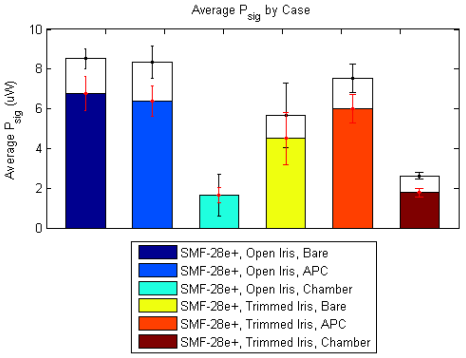

(c) Signal Power

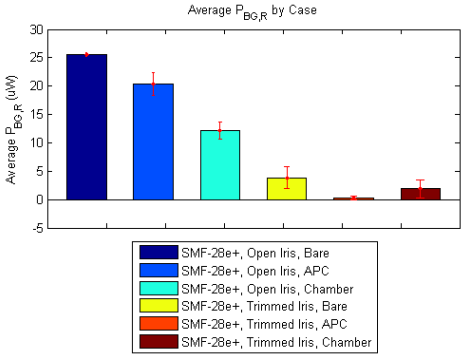

(d) Background Power

Figure A.10: Signal-to-Background Contast Ratio Data, SMF28e+

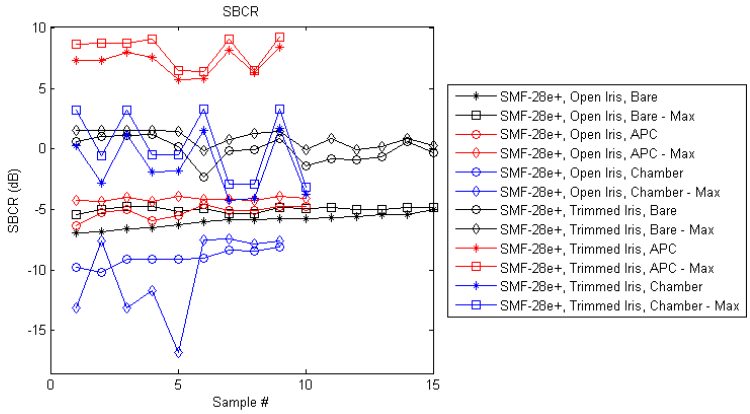

(a) Raw SBCR data

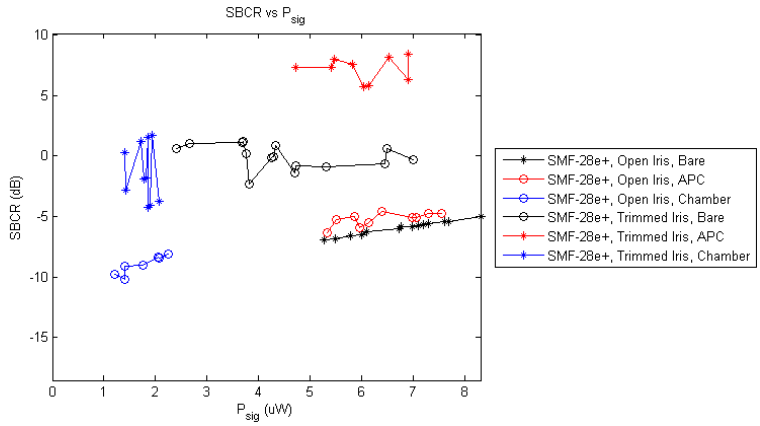

(b) SBCR vs Signal Power

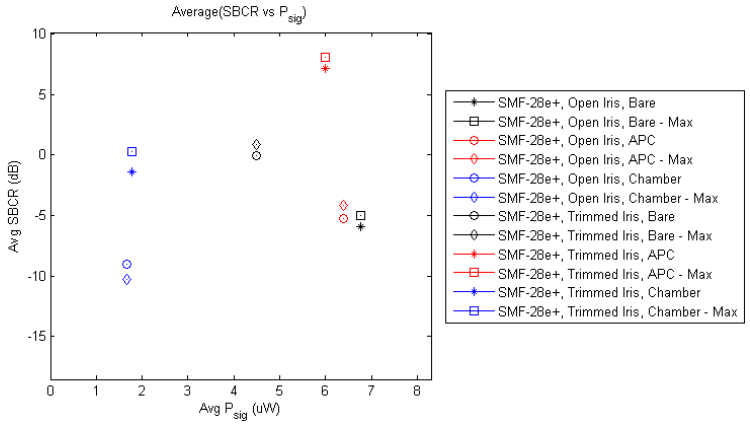

(c) Average SBCR vs Average Signal Power

Figure A.11: Average SBCR

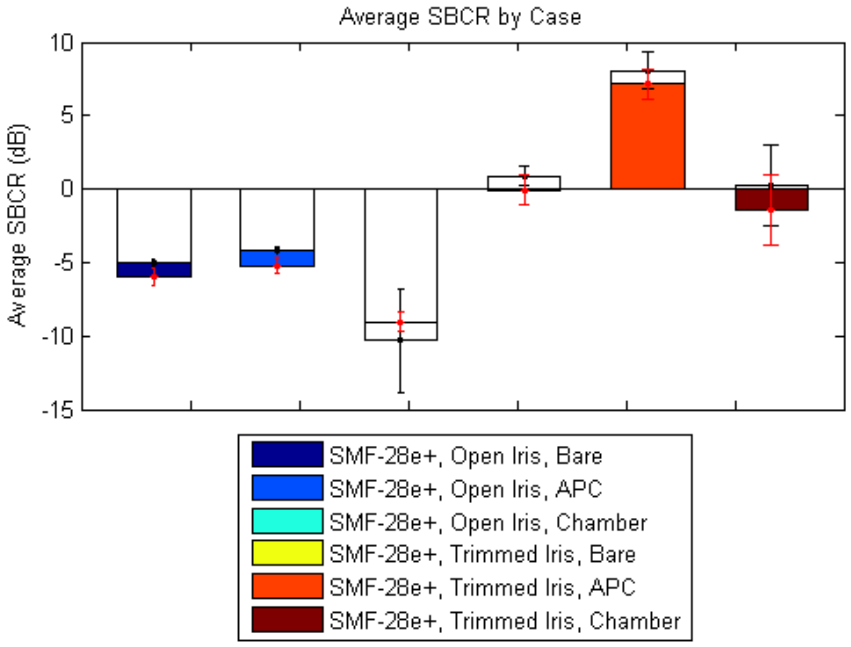

SMF28e+ Chamber/APC Comparison

Figure A.12: Comparison of Chamber and APC Results, SMF28e+

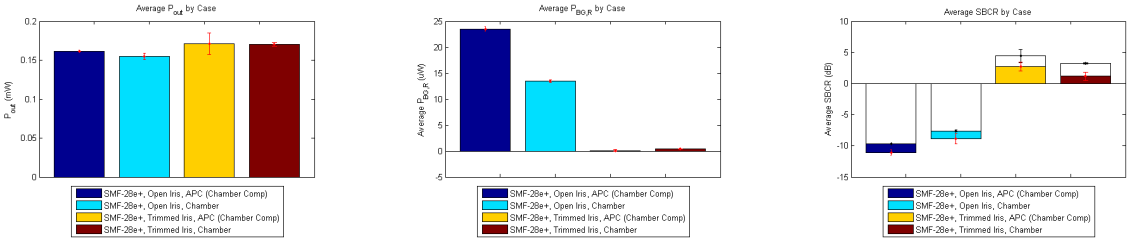

(a) (b) (c)